Chemical Geology 395 (2015) 176–195

Contents lists available at ScienceDirect

Chemical Geology

journal homepage: www.elsevier.com/locate/chemgeo

High-temperature equilibrium isotope fractionation of non-traditional stable isotopes: Experiments, theory, and applications

Edward D. Young [a,*], Craig E. Manning [a], Edwin A. Schauble [a], Anat Shahar [b], Catherine A. Macris [c], Codi Lazar [b], Michelle Jordan [a]

[a] Department of Earth, Planetary, and Space Sciences, UCLA, United States
[b] Geophysical Laboratory, Carnegie Institution of Washington, United States
[c] California Institute of Technology, United States

ARTICLE INFO

Article history:
Received 14 August 2014
Received in revised form 15 December 2014
Accepted 17 December 2014
Available online 26 December 2014

Editor: K. Mezger

Keywords:
Stable isotopes
Magnesium
Silicon
Iron
Core formation

ABSTRACT

High-temperature partitioning of the stable isotopes of rock-forming elements like Mg, Si, Fe, Ni and others are useful new tools in geochemistry and cosmochemistry. Understanding the fundamental driving forces for equilibrium inter-mineral fractionation comes from basic crystal chemistry and is invaluable for interpreting data from natural systems. Both charge and coordination number are key factors affecting bond length and bond stiffness and therefore the relative proclivity of a mineral phase for concentrating heavy or light isotopes. Quantitative interpretation of the plethora of new data relies on refinements of equilibrium fractionation factors through a feedback between crystal chemical reasoning, ab initio predictions, experiments, and analyses of well-characterized natural samples. This multifaceted approach is leading to a rapid rate of discovery using non-traditional stable isotopes in high temperature systems. For example, open-system mass transfer in the mantle is becoming increasingly evident from departures from equilibrium Mg and Fe isotope ratio partitioning between minerals, and differences in isotope ratios between bulk silicate Earth and meteorites are elucidating the conditions for Earth's core formation quantitatively. These applications rely critically on accurate equilibrium fractionation factors.

Contents

1. Introduction

Ratios of the so-called non-traditional stable isotopes (stable isotopes of elements other than the more traditional H, C, N, O, and S) can be used in a variety of ways in the study of rocks formed at

* Corresponding author.
E-mail address: eyoung@epss.ucla.edu (E.D. Young).

http://dx.doi.org/10.1016/j.chemgeo.2014.12.013
0009-2541/

high temperatures. Two of the most common are thermometry, meaning the calculation of temperatures from the distribution of isotopes between phases, and the sorting of parageneses, i.e., the identification of equilibrium (or disequilibrium) mineral assemblages by virtue of their degree of isotopic equilibration (or lack of equilibration) (e.g., Young et al., 2009; Pogge von Strandmann et al., 2011). On a planetary scale, isotope partitioning can be used to infer the presence of unseen reservoirs, light elements in the core being a prominent recent example (Georg et al., 2007; Shahar et al., 2009; Ziegler et al., 2010; Fitoussi and Bourdon, 2012).

Equilibrium isotope fractionation factors between phases are a prerequisite for all of these applications, whether they are being applied to interpret data under the assumption of isotopic equilibrium or as foils for exposing disequilibrium. Even in studies where the aim is to use non-traditional stable isotope ratios as tracers of geochemical reservoirs, as in the mantle for example, where fractionation between phases is not the primary focus, equilibrium isotope fractionation factors are nonetheless indispensible for interpretations of whole-rock data (e.g., Williams and Bizimis, 2014). Determining reliable equilibrium fractionation factors requires feedbacks between computational predictions and experiments. Our experience in the last decade has shown that experiments are required to assess the veracity of computational predictions for the non-traditional stable isotopes. Nonetheless, it is also true that these systems have proven surprisingly amenable to predictions by ab initio calculations. In some cases, natural samples can be used to calibrate fractionation factors where theory is uncertain and experiments are lacking.

A sound appreciation for the sources of inter-mineral isotope partitioning comes from basic crystal chemical principles. Bond strength, or more specifically, bond stiffness, controls vibrational frequencies that in turn influence the propensity for heavier or lighter isotopes to occupy a given crystallographic site. Measurements of mineral isotope fractionations for a variety of major rock-forming in the laboratory and in the field over the last decade have shown that simple crystal chemical considerations can be used to predict the signs and rough magnitudes of inter-mineral isotope fractionation.

In this review we focus on advances in our understanding of high-temperature stable isotope fractionation in the Mg, Si, Fe, and Ni systems with applications in geochemistry and planetary science. This is a rapidly growing field, and by necessity we emphasize those contributions for which we have first-hand knowledge from studies carried out at UCLA and the Geophysical Laboratory.

2. Factors influencing isotope fractionation

2.1. The foundations

Isotope substitution affects the bulk thermodynamic properties of crystalline materials by altering the energy associated with the ever-present vibrational motions of constituent atoms. Equilibrium inter-mineral stable isotope fractionation arises from differences in the effects of atomic mass on vibrational energies in crystals (Bigeleisen and Mayer, 1947; Urey, 1947). Appreciation for the factors controlling fractionation comes from the underlying principles. A complete description of the theory behind stable isotope fractionation can be found in previous reviews (e.g., O'Neil, 1986; Schauble, 2004). Here we present the theory needed to explain the derivation of some basic crystal chemical principles for understanding the sign and overall magnitudes of inter-mineral isotope fractionations presented in Section 2.2.

We can focus exclusively on the energy associated with vibrational motions in the crystalline materials of interest when deriving equilibrium isotope fractionation factors because the energy differences associated with translations cancel at equilibrium, and because in solids, rotations are hindered and so can not contribute to the total energy of motions. The energy of a vibration with frequency ν_i for a particular type of oscillatory motion i (e.g., the stretching motion between a cation and an anion) with quantum number n (with values 0, 1, 2, ...0) can be written as

$$E(n,\nu_i) = \left(n+\frac{1}{2}\right)h\nu_i\left(1-\eta\left(n+\frac{1}{2}\right)\right) \tag{1}$$

where h is the Planck constant and η quantifies departures from harmonicity in the vibrations (a finite value for η related to the energy well depth results in the familiar Morse potential describing potential energy versus inter-atomic separation for a diatomic molecule). For isotope work, it is often assumed that $\eta = 0$ (i.e., it is assumed that the vibration is harmonic). In this case

$$E(n,\nu_i) = \frac{1}{2}h\nu_i + nh\nu_i \tag{2}$$

where the first term on the right-hand side is the zero-point energy (where $n = 0$). The total energy associated with vibrational frequency ν_i is partitioned among the different energy states prescribed by quantum numbers n. The probability for the occurrence of a vibrational energy level corresponding to quantum number n and frequency ν_i, $P(E(n, \nu_i))$, as a function of temperature is calculable from the Boltzmann factor for that energy level:

$$P(E(n,\nu_i)) = \exp\left(-\frac{(n+\frac{1}{2})h\nu_i}{k_\mathrm{b}T}\right) \tag{3}$$

where k_b is the Boltzmann constant. Eq. (3) can be rewritten using the substitution

$$u_i = \frac{h\nu_i}{k_\mathrm{b}T} \tag{4}$$

to obtain

$$P(E(n,u_i)) = e^{-\left(n+\frac{1}{2}\right)u_i}. \tag{5}$$

Because the probabilities in Eq. (5) are exclusive, the total probability for all n, P_{ν_i}, is the sum of the Boltzmann factors over all n:

$$P_{\nu_i} = \sum_{n=0}^{n\sim\infty} e^{-(n+1/2)u_i}. \tag{6}$$

The approximate symbol in front of the infinity symbol in Eq. (6) reminds us that in principle, only in the case of perfectly harmonic vibrations can n go to infinity. Eq. (6) is a geometric series and is evaluated using the general formula for such a series:

$$P_{\nu_i} = \sum_{n=0}^{n=\infty}\left(e^{-u_i}\right)^{\left(n+\frac{1}{2}\right)} = \frac{\left(e^{-u_i}\right)^{1/2}-\left(e^{-u_i}\right)^{\infty}}{1-e^{-u_i}} = \frac{e^{-u_i/2}}{1-e^{-u_i}}. \tag{7}$$

Thus far we have focused on vibrations with a particular frequency corresponding to a particular type of motion. However, there are a multitude of interatomic vibrational motions with different vibrational frequencies in a crystalline material all occurring simultaneously. The total probability for all vibrational frequencies occurring *simultaneously* is the product of probabilities for a single frequency given by Eq. (7). This product is referred to as the vibrational partition function Q_vib:

$$Q_\mathrm{vib} = \prod_i \frac{e^{-u_i/2}}{1-e^{-u_i}}. \tag{8}$$

The numerator in Eq. (8) corresponds to the zero-point energy. The complete partition function Q due to all atomic motions is obtained from the products of translational, rotational, and vibrational partition functions for the case of harmonic oscillations.

A vibrational *mode* is defined by both the frequency of vibration and the wavelength of the lattice wave corresponding to the vibration. The wavelength is determined by the degree to which characteristic motions defining a particular frequency of vibration within adjacent unit cells are in or out of phase with one another. Because unit cells are not isolated molecular units, however, their linkages result in *dispersion* whereby otherwise identical frequencies depend on the wavelength λ of the lattice wave (also referred to as the phonon phase wavelength) to varying degrees. As a result, there will be a large number of modes comparable in number to the number of atoms. Indeed, if n_A is the number of atoms comprising the structure, the product in Eq. (8) is formally over $3n_A$ independent vibrational modes *i*. In practice, the product in Eq. (8) for a crystalline material is taken over at least 3*N* modes where *N* is the number of atoms per unit cell.

Branches are groups of modes usually related by a particular characteristic vibrational motion (symmetric or asymmetric stretching, bending, and so forth). Each mode of a branch is generated by the same basic oscillatory motion but with different lattice wavelengths arising from the degree to which adjacent oscillators are in or out of phase. The 3*N* modes referenced above correspond to the $3N - 3$ optical branches and 3 acoustic branches (Fig. 1). *Optical branches* are analogous to independent intramolecular vibrational modes (Einstein oscillators) where the unit cell plays the role of a molecule. In some cases a single frequency can be used to characterize each optical branch where the branches are identified with a particular motion (Kieffer, 1982), and the number of optical modes to include in the product in Eq. (8) is then $3N - 3$. However, more generally, because of the dispersion whereby the vibrational frequencies for a branch depend on lattice wavelength λ over the Brillouin zone (i.e., over values for the phonon phase wavelength λ from infinity to 2*a* where *a* is the lattice constant) (Fig. 1), the variations in frequency among the modes comprising an optical branch can require sampling many modes per branch in order to evaluate Eq. (8) (i.e., dense sampling of the branch at numerous wave vector values) (e.g., Blanchard et al., 2009). The three acoustical branches, analogous to intermolecular or inter-cell motions in three dimensions, are generally characterized by increasing frequency with decreasing phonon wavelength over the Brillouin zone (Fig. 1). This dependence of acoustic-mode frequencies on wavelength is a first-order result of their inter-cell character; when all unit cells are in phase the lattice wavelength λ = infinity, corresponding to the origin in Fig. 1, and the corresponding acoustic vibration has degenerated into a simple translation. In some cases dispersion can even break the correspondence between a characteristic motion and a branch. An extreme example is when an acoustic branch transitions into an optical branch at shorter wavelengths (leveling off of the higher-frequency acoustic branch in Fig. 1 represents a step towards this phenomenon).

The large range in frequencies associated with acoustic branches can be included in Eq. (8) by integrating the vibrational density of states (number of modes per unit frequency) for the continuum of modes comprising the acoustic branches (Kieffer, 1982) (Fig. 1). In fact, Eq. (8) can be evaluated more generally by taking the logarithm and replacing the resulting sum over vibrational frequencies with an integral that weights each term by the density of vibrational states, yielding

$$\begin{aligned}\ln Q_{\text{vib}} &= \int_0^{\nu_{i,\ \max}} \ln\left(\frac{e^{-u_i/2}}{1-e^{-u_i}}\right) g(\nu_i)\,d\nu_i \\ &= \int_0^{\nu_{i,\ \max}} \left[-\frac{u_i}{2} - \ln\left(1-e^{-u_i}\right)\right] g(\nu_i)\,d\nu_i\end{aligned} \tag{9}$$

where $g(\nu_i)$ is the density of vibrational states (see Kieffer, 1979). The density-of-states function $g(\nu_i)$ is shown for FeO in Fig. 1. Eq. (9) shows that the shape of $g(\nu_i)$ defines the vibrational partition function. This is the basis for extracting isotope fractionation factors from measurements of densities of state using methods like nuclear resonance inelastic X-ray scattering (NRIXS) (e.g., Murphy et al., 2013).

As with any reaction, equilibrium constants for isotope exchange arise from differences in standard-state internal energies that in turn depend on differences in partition functions. The Helmholtz free energy, *F*, is a measure of internal energy where the variables of interest are temperature, volume, and composition (we use volume rather than pressure in this case because we will focus on the temperature effects of isotope fractionation in this derivation, but interest in pressure

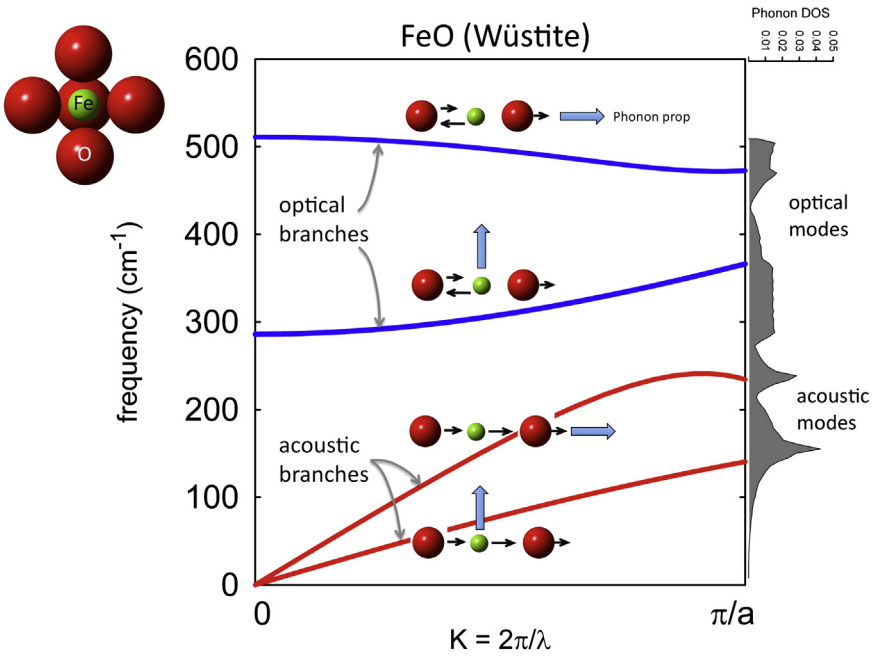

Fig. 1. Phonon dispersion diagram for wüstite (FeO structure shown at top left with the oxygen nearest the observer removed for clarity) based on the data of Kugel et al. (1977). The abscissa is the wave vector ($K = 2\pi/\lambda$) in the [001] direction showing variations in phonon wavelength, λ, in that direction. The ordinate is vibrational frequency. The wüstite structure has two atoms per unit cell so there are a total of six branches (four of which are distinguishable in this section). Optical branches are plotted as blue lines. Acoustic branches are plotted as red lines. Insets show the relative motions of Fe and O atoms (black arrows) to illustrate the vibrational modes for each branch. Blue arrows in the insets show the phonon wave propagation directions relative to the atomic motions; motions parallel to propagation have higher frequencies than motions perpendicular to propagation. At right is the number of modes vs. frequency (the phonon density of states, $g(\nu)$).

isotope effects is growing, as discussed below). The partition function is related to the free energy by $F = -k_b T \ln Q$. For isotope substitution in a single crystalline phase, the difference in internal energy is related to the effect of mass on vibrational energy as expressed by the vibrational partition functions:

$$F'_{vib} - F_{vib} = RT \ln Q_{vib} - RT \ln Q'_{vib} \tag{10}$$

or

$$-\Delta F_{vib} = RT \ln\left(\frac{Q'_{vib}}{Q_{vib}}\right) \tag{11}$$

where the prime symbol designates the quantity with the light isotope replaced by the heavy isotope. The significance of Eq. (11) is most easily conveyed by example. Consider the silicon isotope exchange reaction between quartz and free silicon atoms

$$^{28}SiO_2 + {}^{29}Si \rightleftarrows {}^{29}SiO_2 + {}^{28}Si. \tag{12}$$

The equilibrium constant for this reaction can be written in terms of partition functions. The free atoms in reaction (12) have translational partition functions that can be treated classically and are

$$Q_{trans} = V\left(\frac{2\pi m k_b T}{h^2}\right)^{3/2} \tag{13}$$

where V is the volume for the motion and m is atomic mass. The translational partition function ratio for the isotopic atomic species is therefore

$$\frac{Q'_{trans}}{Q_{trans}} = \left(\frac{m'}{m}\right)^{3/2}. \tag{14}$$

From Eqs. (11) and (14) the equilibrium constant for the reaction in Eq. (12) is seen to be

$$\begin{aligned} K_{Eq} &= \exp(-\Delta F/(k_b T)) \\ &= \frac{Q'_{vib} Q_{trans}}{Q_{vib} Q'_{trans}} \\ &= \frac{Q'_{vib}}{Q_{vib}}\left(\frac{m}{m'}\right)^{3/2}. \end{aligned} \tag{15}$$

The equilibrium constant in Eq. (15) is referred to as the reduced partition function ratio, β, such that

$$\beta = \frac{Q'_{vib}}{Q_{vib}}\left(\frac{m}{m'}\right)^{3/2}. \tag{16}$$

Beta factors are the f values of Bigeleisen and Mayer (1947) modulo symmetry numbers that apply for molecules (more precisely, $\beta = f^{1/n}$ where n is the number of atoms exchanged and is usually 1). Tabulated β values can be used to calculate equilibrium fractionation factors between two phases A and B, α_{A-B}:

$$\alpha_{A-B} = \beta_A / \beta_B \tag{17}$$

where the fractionation factor is the isotope ratio by number for phase A divided by the same ratio for phase B, e.g., $(N'/N)_A/(N'/N)_B$, and where N' and N are the number of the heavy and light isotopes, respectively. In practice, we express fractionations in terms of per mil differences using the approximation that $\delta_A - \delta_B \sim 10^3 \ln(\alpha_{A-B})$ where $\delta_A = 10^3((N'/N)_A/(N'/N)_{Standard} - 1)$ is the isotope ratio of interest expressed as the per mil deviation from a standard value.

For example, the silicon isotope exchange reaction between quartz and pyroxene

$$^{28}SiO_2 + Mg^{29}SiO_3 \rightleftarrows {}^{29}SiO_2 + Mg^{28}SiO_3 \tag{18}$$

has the associated equilibrium constant

$$\begin{aligned} K_{Eq} = \alpha_{SiO_2\text{-}MgSiO_3} &= \frac{\left(N_{^{29}Si}/N_{^{28}Si}\right)_{SiO_2}}{\left(N_{^{29}Si}/N_{^{28}Si}\right)_{MgSiO_3}} \\ &= \frac{\beta_{SiO_2}}{\beta_{MgSiO_3}} \\ &= \frac{Q'_{vib,SiO_2}}{Q_{vib,SiO_2}} \frac{Q_{vib,MgSiO_3}}{Q'_{vib,MgSiO_3}} \left(\frac{m}{m'}\right)^{3/2} \left(\frac{m}{m'}\right)^{-3/2} \\ &= \frac{Q'_{vib,SiO_2}}{Q_{vib,SiO_2}} \frac{Q_{vib,MgSiO_3}}{Q'_{vib,MgSiO_3}}. \end{aligned} \tag{19}$$

In Eq. (19) the equilibrium constant and fractionation factor are one and the same because there is exchange of one silicon between phases containing only one silicon per formula unit. In general where n is the number of atoms of interest exchanged, $\alpha = K_{Eq}^{1/n}$.

Eq. (8) can be used to expand the definition of β in Eq. (16) in terms of vibrational frequencies:

$$\beta = \left(\frac{m}{m'}\right)^{3/2} \prod_i \frac{e^{-\left(h\nu'_i/(k_b T)\right)/2}}{1 - e^{-h\nu'_i/(k_b T)}} \frac{1 - e^{-h\nu_i/(k_b T)}}{e^{-(h\nu_i/(k_b T))/2}}. \tag{20}$$

Eq. (20) can be rewritten to omit the translational partition function ratio for atoms by recognizing that this term must be equivalent to the product of vibrational frequency ratios u_i'/u_i (Kieffer, 1982). This constraint, also referred to as the high-temperature product rule, is a manifestation of conservation of momentum and is necessary for the disappearance of isotope partitioning in the limit of high temperatures. The same result, but with the symmetry numbers that do not apply for crystalline structures, is obtained for unbound molecules using the Redlich–Teller isotopic product rule that accounts for rotational motions (Urey, 1947; Pupyshev et al., 1994). Using the product rule, Eq. (20) becomes

$$\beta = \prod_i \frac{h\nu'_i/(k_b T)}{h\nu_i/(k_b T)} \frac{e^{-\left(h\nu'_i/(k_b T)\right)/2}}{1 - e^{-h\nu'_i/(k_b T)}} \frac{1 - e^{-h\nu_i/(k_b T)}}{e^{-(h\nu_i/(k_b T))/2}}. \tag{21}$$

Although having the advantage of being written entirely in terms of vibrational frequencies, Eq. (21) is not especially useful for gaining an intuitive appreciation for the factors that control equilibrium partitioning between phases. For high temperatures where u_i are relatively small, a more revealing form can be obtained by approximation (Bigeleisen and Mayer, 1947; Urey, 1947). Firstly, some algebraic manipulation yields

$$\beta = \prod_i \frac{u'_i}{u_i} \frac{1}{e^{u'_i/2} - e^{-u'_i/2}} \frac{e^{u_i/2} - e^{-u_i/2}}{1}. \tag{22}$$

Because $\mathrm{csch}(x) = 2/(e^x - e^{-x})$ and $\sinh(x) = (e^x - e^{-x})/2$ we rewrite Eq. (22) as

$$\beta = \prod_i \frac{u'_i}{u_i} \frac{\mathrm{csch}(u'_i/2)}{2} 2\sinh(u_i/2). \tag{23}$$

Substitution of the Taylor series approximations for the hyperbolic functions truncated after two terms, $\mathrm{csch}(x) \sim 1/x - x/6$ and $\sinh(x) \sim x + x^3/3$!, results in

$$\begin{aligned}\beta &= \prod_i \frac{u_i'}{u_i}\frac{1}{2}\left(\frac{2}{u_i'} - \frac{u_i'}{12}\right)2\left(\frac{u_i}{2} + \frac{u_i^3}{48}\right)\\ &= \prod_i \frac{u_i'}{u_i}\left(\frac{1}{u_i'} - \frac{u_i'}{24}\right)\left(u_i + \frac{u_i^3}{24}\right)\\ &= 1 + \frac{1}{24}\sum_i \left(u_i^2 - u_i'^2\right)\end{aligned} \tag{24}$$

where products of u_i and u_i' with order greater than 3 have been neglected.

The $\sum_i \left(u_i^2 - u_i'^2\right)$ term in this so-called "1 over 24" approximation shown in Eq. (24) can be expanded further to arrive at a more explicit equation for isotope fractionation. Eq. (24) shows that the effect of isotope substitution in a crystalline material is expressed by the difference in the squares of the frequencies of vibration for the isotopologues. Treating the vibrations as harmonic allows us to invoke Hooke's law and introduces the force constants that dictate the frequencies of motions:

$$\nu_i = \frac{1}{2\pi}\sqrt{\frac{K_{f,i}}{\mu_i}} \tag{25}$$

where μ_i is the reduced mass. Bigeleisen and Mayer (1947) showed that if the atom of interest is treated as experiencing restoring forces in three principal directions while the other atoms comprising the structure are treated as stationary, a single effective force constant, K_f, that is independent of the isotope substitution, can be used in evaluating Eq. (24). If there is more than one crystallographic site for the atom of interest one can obtain an average force constant for the sites, $\hat{K}_f$. This is similar in principle to obtaining an average force constant using a phonon density of states. Substitution of Eqs. (4) and (25) into (24) for a single effective restoring force constant gives

$$\beta = 1 + \frac{1}{24}\left(\frac{h}{k_b T}\right)^2 \frac{\hat{K}_f}{4\pi^2}\left(\frac{1}{\mu_i} - \frac{1}{\mu_i'}\right). \tag{26}$$

From the definition of reduced mass it is straightforward to show that the difference in reciprocal reduced masses is the same as the difference in reciprocal atomic masses, m_i, (Young et al., 2002) allowing the latter to be factored thusly

$$\beta = 1 + \frac{1}{24}\left(\frac{h}{k_b T}\right)^2 \left(\frac{1}{m} - \frac{1}{m'}\right)\frac{\hat{K}_f}{4\pi^2}. \tag{27}$$

We can use this equation to write equations for isotope fractionation factors between two minerals A and B, α_{A-B}.

Towards this end, from Eq. (17) we have

$$\ln\alpha_{A-B} = \ln\beta_A - \ln\beta_B \tag{28}$$

and from the approximation $\ln(1 + x) \cong x$ for small x we finally arrive at

$$\ln\alpha_{A-B} = \frac{1}{24}\left(\frac{h}{k_b T}\right)^2 \left(\frac{1}{m} - \frac{1}{m}\right)\left[\frac{\hat{K}_{f,A}}{4\pi^2} - \frac{\hat{K}_{f,B}}{4\pi^2}\right]. \tag{29}$$

Eq. (29) is useful because it shows explicitly that isotope fractionation between two phases at high temperatures ($T >> 300$ K) depends on the inverse of the square of temperature, on the difference in mass between the two isotopes, and on the differences in force constants for the vibrational modes in each phase. It also shows clearly that the greater force constants concentrate the heavier isotopes; where relevant force constants for phase A are greater than for phase B, $\alpha_{A-B} > 1$. Said another way, stiff bonds favor heavy isotopes in order to reduce the relatively high frequency of vibration. Eq. (29) shows explicitly that understanding fractionation means understanding the factors that control bond force constants.

2.2. Crystal chemical controls on fractionation

Ab initio calculations provide the means to calculate fractionation factors. However, these calculations in and of themselves may not convey an understanding of the crystal chemical controls on fractionation except to the model practitioners. We have found that basic crystal chemical principles can be used to assess, qualitatively or semi-quantitatively, the force constants in Eq. (22) and thus the fractionation between mineral phases. These principles, rooted ultimately in Pauling's rules, help guide the selection of natural samples for analysis and help the design of experiments for evaluating fractionation in the laboratory.

Pauling's rules have proven useful for understanding crystal structures since their introduction (Pauling, 1929, 1960). While originally based on the precepts of ionic structures, these rules remain effective in rationalizing, and even predicting, structures and site occupancies in silicate and oxide minerals (Burdett and McLarnan, 1984; Burdett and Hawthorne, 1993). Burdett and McLarnan (1984) showed that predictions from Pauling's rules can be understood in the topological framework of band structure. The character of the bond, either covalent or ionic, does not enter into application of Pauling's rules (Burdett and Hawthorne, 1993; Gibbs et al., 2014a). Rather, the rules are a "useful fiction" (Hazen, 1988) where nearest neighbor bonding is important.

We can make use of Pauling's rules for stable structures to provide a picture of the crystal chemical factors controlling isotope fractionation beginning with a Born–Mayer type interionic potential (Born and Mayer, 1932) for the bond. One can compute the force constants required for Eq. (29) by differentiation of the corresponding interionic forces:

$$K_f = \frac{\partial}{\partial r_{ij}}\left(-\frac{z_i z_j e^2}{4\pi\varepsilon^o r_{ij}^2} - \frac{nb}{r_{ij}^{n+1}}\right) \tag{30}$$

where z_i and z_j are the cation and anion valences, e is the charge of an electron, ε^o is the vacuum permittivity, r_{ij} is the interionic spacing, and b and n are the Born–Mayer constants for the repulsion term (throughout what follows we adopt an empirical value of 12 for n while b is determined by measured equilibrium interionic distances). By evaluating the constants at the equilibrium interionic distance r_o it is straightforward to show that

$$K_f = \frac{z_i z_j e^2(1-n)}{4\pi\varepsilon^o r_o^3}. \tag{31}$$

We gain insight by introducing into the force constant the concept of the "mean bond strength", $\bar{s}_i$, for an ionic species i as defined by Pauling (1929):

$$\bar{s}_i = \frac{z_i}{\upsilon_i} \tag{32}$$

where z_i is the valence of the atom of interest and υ_i is the number of coordinating species (e.g., number of nearest neighbor oxygens surrounding a cation). Pauling's second rule for stable structures states that the sum of mean bond strengths should equal the valence of the coordinated ion. For example, if ξ is the valence of an anion, the sum of mean bond strengths over the nearest-neighbor bonded cations should satisfy $\xi = \sum_i \bar{s}_i$. Accordingly, values of $\bar{s}_i$ measure the fractional charge donated by the cation to the anion and vice versa. This is in essence a measure of electron density between bond partners and

represents the parsing of bond potential between nearest neighbors (Gibbs et al., 2014a,b). As an example, consider that the Si-O bond in silicates is only ~51% ionic (Pauling, 1980), and estimates for the effective charge on the Si^{4+} and O^{2-} ions range from +1.0 to +3.2 and −0.5 to −1.8, respectively (Stewart et al., 1980; Fujino et al., 1981; Detraux and Gonze, 2001; Kirfel et al., 2005). And yet, Pauling's second rule still holds for silicates: e.g., in the quartz structure, the sum of the charges donated by each of the four oxygen's surrounding silicon sum to the ionic charge of the silicon $(4| - 2/2| = 4$, where each oxygen is coordinated by 2 cations and 4 is the formal charge for Si). General, if sometimes imperfect, adherence to $\xi = \sum_i \bar{s}_i$ applies to the other sites in silicates as well.

Because the logarithms of Pauling's bond strengths correlate well with bond lengths, one can build Pauling's rules into the ionic equation for force constants by using effective ionic radii to estimate interionic distances in Eq. (24) (Shannon, 1976). A recent review of the accuracy of these effective radii in the context of electron density distributions is given by Gibbs et al. (2014a). The effective radii vary positively with coordination number and negatively with charge, exerting the primary controls on the differences in force constants that drive isotope fractionation. The variations in bond length with coordination and valence, and the sensitivity of force constants on the bond lengths require that, all else equal

1. *Heavy isotopes concentrate where coordination number is low, and*
2. *Heavy isotopes concentrate where valence is high.*

Both of these rules follow from the propensity of heavy isotopes to concentrate where force constants are greatest, and therefore in stiffer bonds. We have found these rules to be successful in predicting the sign and often the relative magnitudes of fractionation factors for the isotopes of rock-forming elements, including Mg, Si, and Fe.

2.3. Examples

Ionic models provide estimates of fractionation factors that are within a factor of ~2 or 3 of ab initio calculations (e.g., Density Functional Theory, DFT) or experiments, and often considerably better. More importantly, they provide a useful framework for understanding the causes of stable isotope fractionation. In applying ionic principles we find that the simple calculations using a single average bonding environment from weighted sums of effective ionic radii in Eq. (31) are best. Use of Eq. (31) should be contrasted with the earlier approach by Young et al. (2009) in which the ionic charges in Eq. (31) were replaced by mean bond strengths from Eq. (32). This latter formulation generally underestimates fractionation factors and should be supplanted by the simpler method described here (i.e., Eq. (31) should be used to estimate force constants without modification). Averaging force constants given by Eq. (31) works well because the effective ionic radii correlate so well with electron density, a first-order measure of bond characteristics (Gibbs et al., 2014b). The relative successes and failures of predictions for the Mg, Si and Fe isotopic systems serve as examples of the usefulness of a crystal chemical perspective on fractionation. Comparisons like those highlighted here hone our understanding of the sources of inter-mineral isotope fractionation and would not be possible without significant advances in computational and experimental methods over the last ten years.

The calculated fractionation factor for $^{26}Mg/^{24}Mg$ between spinel ($MgAl_2O_4$) and forsterite (Mg_2SiO_4) serves as an example. Because Mg in spinel is in four-fold coordination while it is in six-fold coordination in forsterite (Fig. 2), we expect that $^{26}Mg/^{24}Mg$ will be significantly greater for spinel than for forsterite at isotopic equilibrium because of the shorter Mg-O bond lengths for tetrahedral Mg (^{IV}Mg-O effective bond length = 0.195 nm) compared with octahedral Mg (^{VI}Mg-O effective bond length = 0.210 nm). Fig. 3 compares results of experiments (Macris et al., 2013), DFT calculations (Schauble, 2011), and Eqs. (29) and (31) using the effective ionic radii of Shannon

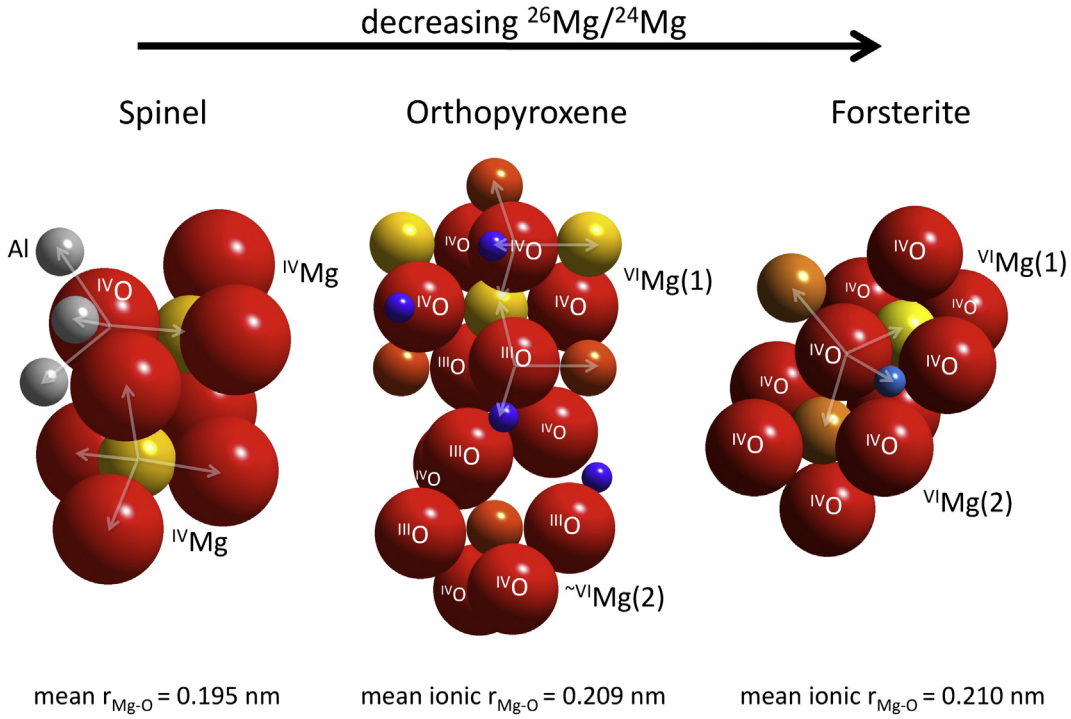

Fig. 2. Crystal structures for spinel ($MgAl_2O_4$), orthopyroxene ($MgSiO_3$), and forsterite (Mg_2SiO_4) showing nearest neighbors that influence Mg isotope fractionation. Structures are depicted using ionic radii of Shannon (1976). Oxygen is shown as large red spheres, magnesium is shown as green spheres (M1 site) or orange spheres (M2 site), silicon as blue spheres, and aluminum as silver spheres. Translucent arrows show examples of bonding to nearest neighbors defining the coordination spheres of interest. All oxygens in spinel and olivine are ^{IV}O while oxygen exists as ^{III}O as well as ^{IV}O in pyroxene. The fractionation between spinel and the other phases is largest due to ^{IV}Mg in spinel. A small preference for higher $^{26}Mg/^{24}Mg$ in pyroxene relative to forsterite derives from shorter bond lengths for Mg–^{III}O vs. that for Mg–^{IV}O. Mean Mg–O bond lengths based on sums of effective radii are shown at bottom.

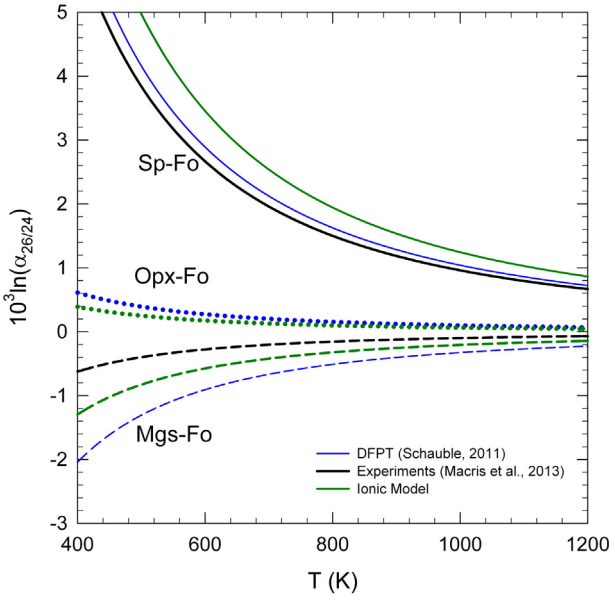

Fig. 3. Comparison of $^{26}Mg/^{24}Mg$ fractionation factors between magnesite and forsterite (Mgs–Fo, dashed lines), orthopyroxene and forsterite (Opx–Fo, dotted lines), and magnesian spinel and forsterite (Sp–Fo, solid lines). Results from experiments (Macris et al., 2013) are shown as black lines, results from density functional perturbation theory (DFPT, Schauble, 2011) are shown as blue lines, and predictions from the ionic models (Eqs. (22) and (24)) are shown as green lines for each mineral pair.

(1976). It is clear that our expectations from crystal chemistry are matched by both experiments and *ab initio* calculations.

The origin of magnesium isotope fractionation between orthopyroxene (enstatite) and olivine (forsterite) is more subtle. In this case Mg exists in octahedral coordination in both phases, and the difference in Mg–O bond lengths, to first order and ignoring distortion of the M2 site, derives from the differences in oxygen coordination (Fig. 2). Oxygen in olivine is in 4-fold coordination (^{IV}O). In orthopyroxene, the octahedral M1 cation sites are coordinated by four ^{IV}O and two ^{III}O atoms (Fig. 2). The distorted M2 site can be thought of as having 3 of 6 (neglecting the ~7th oxygen that is arguably a nearest neighbor) coordinating oxygens as ^{III}O (Fig. 2) and so we average these two bonding environments in applying Eqs. (22) and (24). Because, ideally, the Mg–^{III}O bond (0.208 nm) is shorter than the Mg–^{IV}O bond (0.210 nm), one would predict that orthopyroxene should have higher $^{26}Mg/^{24}Mg$ than coexisting olivine at equilibrium. The close match between DFT calculations and the simple predictions from ionic radii in Fig. 3 shows that this expectation is valid (and compares well with natural samples as discussed in Section 4).

Fractionation of $^{26}Mg/^{24}Mg$ between magnesite and forsterite is complicated by the tightly bound CO_3 groups in the former. We can use the Mg–O bond length calculated from DFT by Schauble (2011) and apply it to Eq. (31). Here the effect of the longer bond is confirmed both by experiments and ab initio calculations, as shown in Fig. 3. In this case the ionic model using the DFT bond length as input splits the difference between the experimental results and the DFT calculations, but in all cases the signs agree and the magnitudes are within a factor of < 3 of one another.

The relative success of the ionic model in predicting the first-order Mg isotope fractionation trends among silicates and oxides, and even carbonates with some help from a priori information about bond lengths, is evidently due to the fact that the electronegativity difference of 2.3 between Mg and O is so large that the bond lengths and charges can be reasonably represented by the empirical ionic radii. The difference in electronegativity between Fe and O is only 1.7, so it is instructive to see how well we can use the principles outlined above to predict features of Fe isotope fractionation between minerals at high temperatures.

Ab initio calculations for inter-mineral iron isotope fractionation are complicated by the electronic structure of iron and fewer results are available for comparisons with natural samples. Nonetheless, it turns out that where detailed models and experiments are lacking, observations from natural samples can be assessed using simple crystal chemical principles. For example, iron isotope fractionation between ferrous iron in garnet and clinopyroxene is expected to be relatively large because of the difference in number of nearest-neighbor oxygens surrounding iron. Ferrous iron occurs as $^{VIII}Fe^{2+}$ in garnet (where we confine ourselves to the almandine component rather than the andradite component) while in pyroxene it exists as $^{VI}Fe^{2+}$. Therefore, all else equal, pyroxene should have higher $^{57}Fe/^{54}Fe$ than almandine garnet at equilibrium by virtue of shorter Fe–O bond lengths. Accounting for this difference in coordination through the Fe–O bond length in Eq. (31) yields the predicted temperature-dependent fractionation shown in Fig. 4. For comparison, Williams et al. (2009) report a 0.4‰ difference in $^{57}Fe/^{54}Fe$ between coexisting clinopyroxene and garnet (Cpx > Grt) with an average estimated equilibration temperature of 1450 K. The ionic model prediction for the fractionation at that temperature is 0.39‰. Based on the single observation from the xenoliths one can infer the temperature-dependent fractionation (e.g., Eq. (29)) to be $10^3\ln\alpha_{57/54} = 8.50 \times 10^5/T^2$ while the ionic model gives $10^3\ln\alpha_{57/54} = 8.17 \times 10^5/T^2$. Beard and Johnson (2004) report differences in $^{57}Fe/^{54}Fe$ between coexisting Cpx and Grt ranging from 0.62 +/− 0.06‰ at a cation equilibration temperature of 1090 K in ecologites to 0.35 +/− 0.09 at 1380 K in garnet peridotite. These values are also in good agreement with the ionic model and with the data from Williams et al. (2009). Close agreement between the fractionation expected based on the difference in coordination expressed as ionic bond lengths and the xenolith data is shown in Fig. 4.

Analogous to the situation with Mg, Fe isotope fractionation for Fe^{2+} between clinopyroxene and olivine is predicted to be small and positive (e.g., $\delta^{57}FeO_{Cpx} > \delta^{57}Fe_{Oliv}$) based on the presence of ^{III}O in pyroxene and its absence in olivine, and on the ordering of Fe^{2+} to the M1 site. This

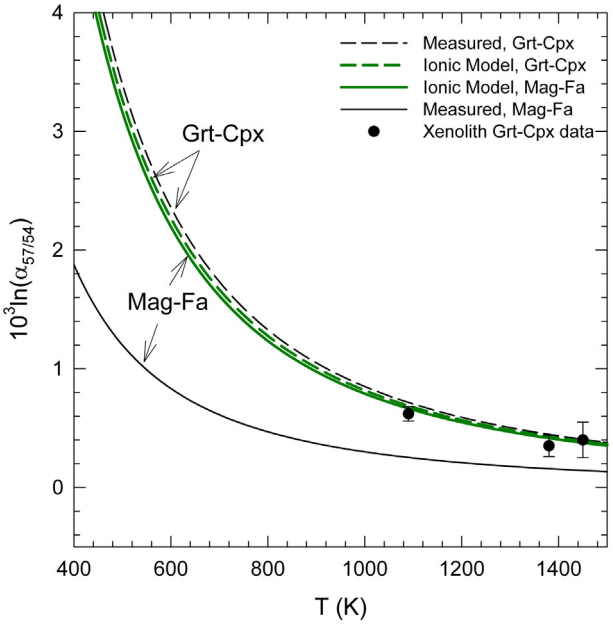

Fig. 4. Comparison of $^{57}Fe/^{54}Fe$ fractionation factors between magnetite and fayalite (Mag–Fa, solid lines) and garnet and clinopyroxene (Grt–Cpx, dashed lines). Results from experiments for Mag–Fa (Shahar et al., 2008) are shown as the black solid line while the prediction for Mag–Fa from the ionic model (Eqs. (22) and (24)) is shown as the green solid line. The temperature-dependent fractionation factors inferred from measurements of Grt–Cpx from eclogite mantle xenoliths (Williams et al., 2009) are shown as the black dashed line and the ionic model Grt–Cpx fractionation is shown as the green dashed line. Mantle xenolith Grt–Cpx fractionations measured by Williams et al. (2009, highest-T point) and Beard and Johnson (2004) are shown as solid black data points.

prediction is qualitatively consistent with the data for these mineral pairs reported in the literature (Beard and Johnson, 2004; Williams et al., 2005; Zhao et al., 2010, 2012), although significant discrepancies exist (see Section 4.1). Macris et al. (2015) made use of the ionic model to predict iron isotope fractionation between orthopyroxene and olivine taking into account Fe^{2+} occupancy of both the M1 and the highly distorted M2 sites in Opx. They predict $\delta^{57}FeO_{Opx}$ to be slightly lower (by < 0.1‰ at relevant equilibration temperatures) than $\delta^{57}Fe_{Oliv}$ at equilibrium *if* all iron is ferrous. Their results are consistent with predictions from the kinetic energy associated with Fe vibrations based on Mössbauer data (Polyakov and Mineev, 2000), although discrepancies between the Mössbauer-based fractionation factors and experiments are discussed in Section 4.1. More quantitative comparisons between predicted fractionation factors and literature data requires accommodation for the presence of ferric iron, as described below.

The iron system is instructive as to the roles of charge and coordination in determining fractionation factors. Experimental and theoretical investigations of iron isotope fractionation in aqueous ferric chloride complexes by Hill et al. (2009) show that ligand identity (in this case H_2O vs. Cl) produces fractionations among species with magnitudes similar to those caused by changes in iron oxidation state. These experiments underscore the conclusions from the garnet-clinopyroxene fractionation example described above that while oxidation state is often touted as the primary driver for iron isotope fractionation (Johnson et al., 2013), bond length differences due to coordination are also important where they exist. We note that coordination and charge are not necessarily orthogonal parameters in crystal chemistry — the higher charged ion (again treating the bonding as ionic for expediency of discussion) is effectively smaller and tends to occupy lower-coordination crystallographic sites, as in the case of garnet.

Iron isotope fractionation between magnetite and fayalite (or the fayalite component in olivine) provides a case study in inter-mineral fractionation arising from both charge and coordination number. Magnetite is an inverse spinel with structural formula $^{IV}(Fe^{3+})^{VI}(Fe^{2+}\ Fe^{3+})^{IV}O_4$ while fayalite has the formula $^{VI}Fe^{2+}{}_2{}^{IV}Si^{IV}O_4$. Inspection of these formulae shows that magnetite is expected to favor the heavy isotopes of iron relative to fayalite because some iron exists in a four-fold crystallographic site, raising the Fe–O force constant and shortening the bond, and because iron also exists as Fe^{3+} rather than just Fe^{2+}, again increasing the Fe–O force constant and shortening the bond. Based on formal charges and ionic radii alone (using high spin configurations for Fe in all cases), the predicted fractionation turns out to be approximately 2× the fractionation measured in the laboratory (Shahar et al., 2008) (Fig. 4).

Even small amounts of ferric iron should have significant effects on inter-mineral Fe isotope fractionation factors. Macris et al. (2015) used the ionic model to predict that an Fe^{3+} / (Fe^{3+} + Fe^{2+}) of ~ 0.2 in clinopyroxene (where coexisting olivine is essentially Fe^{3+} free), a value typical of some San Carlos xenoliths, should greatly enhance $\delta^{57}FeO_{Cpx}$ relative to $\delta^{57}Fe_{Oliv}$ (Fig. 5). Small concentrations of ferric iron might explain the relatively high $\delta^{57}FeO_{Cpx}$ values compared with $\delta^{57}Fe_{Oliv}$ commonly reported in the literature (Fig. 5).

Silicon presents a particular challenge to applications of ionic models for bonding in crystalline materials because of the significant covalency of the Si-O bond. The basic principles, however, still apply. For example, in the case of the $^{30}Si/^{28}Si$ fractionation between quartz and olivine, consideration of the structures of the two phases suggests that the crystal chemical driver for the partitioning should come from differences in oxygen coordination (confining the discussion to ^{IV}Si that dominates in silicates at crustal and upper mantle pressures). Sharing of apical oxygen atoms among all $^{IV}SiO_4$ tetrahedra in quartz (a tectosilicate) leads to two-fold coordination for oxygen, ^{II}O, while isolated $^{IV}SiO_4$ tetrahedra and bonding with neighboring Mg leads to ^{IV}O in forsterite olivine (an orthosilicate). In order to quantify the effect using a simple ionic model, one must accommodate the greater

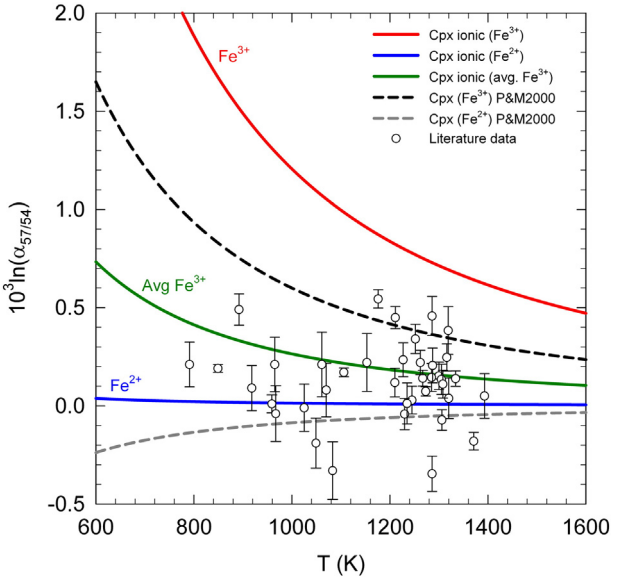

Fig. 5. Temperature-dependent $^{57}Fe/^{54}Fe$ fractionation factors between clinopyroxene (Cpx) and olivine (Oliv) compared with data from the literature where $10^3\ln(\alpha_{57/54}) \sim \delta^{57}Fe_{Cpx} - \delta^{57}Fe_{Oliv}$. Solid curves are ionic model calculations. All calculations are for Fe^{2+}only in Oliv. Lowermost solid curve (blue) is for all Fe^{2+} in Cpx, uppermost solid curve (red) is for all Fe^{3+} in Cpx, and middle solid curve (green) is for average Fe^{3+} / (Fe^{2+} + Fe^{3+}) = 0.2 in Cpx as reported by Macris et al. (2015). Dashed curves are predictions from the Mössbauer data of Polyakov and Mineev (2000) for Fe^{2+} in Cpx (gray) and Fe^{3+} in Cpx (black). The isotope data (open symbols) are for mantle xenoliths as reported by Williams et al. (2005), Zhao et al. (2010, 2012), and Macris et al. (2014). Error bars are 2σ. Temperatures for the xenoliths were calculated using various spinel-olivine and spinel–orthopyroxene-olivine cation exchange thermometers (see Macris et al.,2015 for details).

covalency in the Si–O bond as compared with, for example, the Mg–O bond. Accordingly, and for illustration purposes, one can adopt intermediate effective charges identified by studies of electron densities in order to apply Eqs. (22) and (24). In Fig. 6 we use effective charges of +1.8 and −1.8 for ^{IV}Si and O, respectively (Fujino et al., 1981; Detraux and

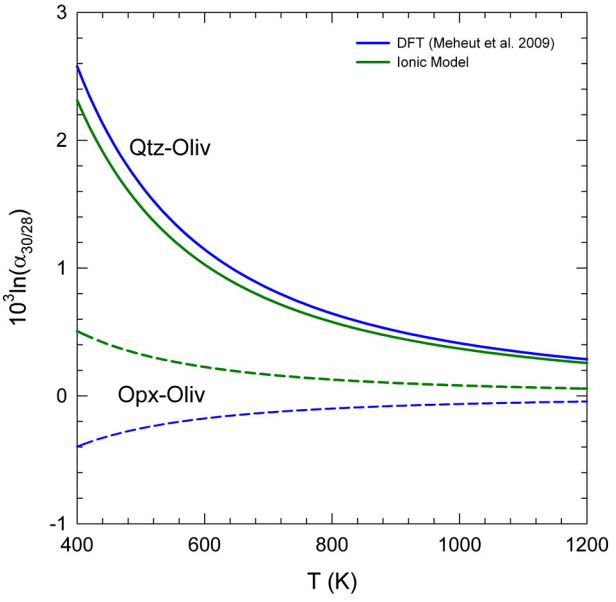

Fig. 6. Calculated $^{30}Si/^{28}Si$ fractionation factors between quartz and olivine (Qtz–Oliv, solid lines) and orthopyroxene and olivine (Opx–Oliv, dashed lines). Results from DFT calculations from Méheut et al. (2009) are shown as blue lines and results from the ionic model are shown as green lines.

Gonze, 2001; Kirfel et al., 2005) to compare the temperature-dependent $^{30}Si/^{28}Si$ fractionation predicted by Eqs. (29) and (31) with the DFT calculations of Méheut et al. (2009). The agreement, although in part fortuitous given the uncertainties surrounding assignments of effective charges, validates our expectations from basic crystal chemistry that the tectosilicate, by virtue of its lower coordination number for oxygen bonded to silicon, should favor the heavy isotopes of Si relative to the orthosilicate with higher coordinated oxygens. Georg (2006) measured a $^{30}Si/^{28}Si$ fractionation between quartz and zircon of 0.34 +/− 0.05‰ in the Laurel Mtn. pluton (Sierra Nevada, CA, USA). This high-temperature fractionation between quartz and another orthosilicate with four-fold coordination of oxygen, zircon, is consistent with the Qtz–Oliv fractionation shown in Fig. 6 in suggesting a reasonable equilibration temperature for a granodiorite near 1000 K (727 °C).

Silicon isotope fractionation between orthopyroxene and olivine at equilibrium should be small for the reason that the differences in oxygen coordination are small. As described above, in olivine oxygen occurs as ^{IV}O while in orthopyroxene the oxygen occurs as 2/3 ^{IV}O and 1/3 ^{III}O. The subordinate ^{III}O, yielding a slightly shorter Si–O bond, would be expected to be a first-order source of a small fractionation with $^{30}Si/^{28}Si$ greater in Opx than in Oliv. This expected fractionation is compared with the more rigorous DFT calculations of Méheut et al. (2009) in Fig. 6. Although the DFT calculations do yield a small fractionation, as one would predict based on the structures of the two phases, the sign is different with a slight favoring of the heavy isotopes of Si in olivine. Méheut and Schauble (2014) discuss the influences of various cations on mean Si–O bond lengths and the departure of forsterite olivine from the well-defined negative correlation between $^{30}Si/^{28}Si$ and Si–O bond length defined by other minerals. This example illustrates the limitations of simple crystal chemical arguments.

Figs. 3, 4, 5, and 6 illustrate that reasonable inferences about signs and magnitudes of fractionations at high temperatures for non-traditional stable isotopes can be obtained from relatively simple crystal chemical constraints. For greater accuracy, a combination of experiments, ab initio calculations, and observations in well-characterized natural samples are required. In Section 3 we discuss one method for obtaining equilibrium fractionation factors at high temperatures used in our laboratories over the past few years.

2.4. Pressure

In recent years the effect of pressure on stable isotope fractionation has become a topic of considerable interest because of the potential for using isotope fractionation as a monitor of planetary differentiation. With a few notable exceptions (e.g., Horita et al., 1999), pressure had not been regarded as a primary driver for stable isotope fractionation historically (Clayton et al., 1975). The reason is the small change in volume associated with moderate changes in pressure. For exchange of a single atom the fractionation factor is an equilibrium constant for the isotope exchange reaction between two phases, allowing us to write the equation for the effect of pressure on fractionation as

$$\left(\frac{\partial\left(10^3\ln\alpha\right)}{\partial P}\right)_T = -\frac{10^3\Delta\hat{V}}{RT} \tag{33}$$

where $\Delta\hat{V}$ is the molar volume change associated with the isotope exchange reaction. Although the volume changes with isotope substitution between phases are indeed small, the effects can be significant at tens to hundreds of GPa (Murphy et al., 2013) and so become potentially significant on planetary scales.

In general, compression stiffens bonds, enhancing frequencies of vibration and amplifying fractionation. This can be illustrated by considering the relationship between vibrational frequency and volume (Grüneisen, 1912):

$$\frac{\nu_i}{\nu_i^o} = \left(\frac{V}{V^o}\right)^{-\gamma_i} \tag{34}$$

where γ_i is the mode Grüneisen parameter, subscript i refers to a mode of vibration and the superscript ^{o} refers to a reference pressure (e.g., room pressure). Since γ_i is of order unity, vibrational frequencies are inversely proportional to volume; greater frequency of vibration with smaller volume is a manifestation of stiffening of bonds with pressure. The shift in frequency with compression is therefore $\Delta\nu_i = \nu_i^o\left(V/V^o\right)^{-\gamma_i} - \nu_i^o$ or $\Delta\nu_i/\nu_i^o \sim -\Delta V/V^o$ when $\gamma_i \sim 1$. Increasing the force constants in Eq. (29) will in general increase fractionation. To see this explicitly, consider that isotope fractionation depends on the square of the differences in frequency incurred by isotope substitution. In the simplified case where the changes in frequency are identical for all vibrational modes in a phase (i.e., $\Delta\nu_1 = \Delta\nu_2 = \ldots = \Delta\nu$, or $\gamma_1 = \gamma_2 = \ldots = \gamma$) we have at pressure

$$\begin{aligned}\ln\alpha_{A\text{-}B} &= \frac{1}{24}\left(\frac{h}{k_bT}\right)^2\left[\sum_i\left\{(\nu_i+\Delta\nu)_A^2-(\nu_i'+\Delta\nu)_A^2\right\}-\sum_i\left\{(\nu_i+\Delta\nu)_B^2-(\nu_i'+\Delta\nu)_B^2\right\}\right]\\ &= \ln\alpha_{A\text{-}B}^o+\frac{1}{24}\left(\frac{h}{k_bT}\right)^2\left[\sum_i\left\{2\Delta\nu_A(\nu_i-\nu_i')_A\right\}-\sum_i\left\{2\Delta\nu_B(\nu_i-\nu_i')_B\right\}\right]\end{aligned} \tag{35}$$

where one can see by inspection (and comparison with Eq. (24)) that there is an additional term that arises upon compression that adds to the magnitude of the fractionation at low pressure ($\ln\alpha_{A\text{-}B}^o$) and that is inversely proportional to volume. We therefore expect $\ln\beta$ to be enhanced with pressure all else equal. For example, this increase has been measured for metallic iron and for iron oxides recently at pressures up to 171 GPa (Polyakov, 2009; Murphy et al., 2013).

Pressure will also induce a change in fractionation behavior due to a change in spin state. Deep in the mantle, ferrous iron in minerals can undergo a partial or complete transition from high- to low-spin state due to compression (Li et al., 2004; Lin et al., 2005), shifting two electrons from antibonding orbitals to bonding orbitals, stiffening the Fe–O bond, and reducing the bond length. Rustad and Yin (2009) used DFT calculations to examine this effect at pressures relevant to Earth's deep interior for ferropericlase ($Fe_xMg_{1-x}O$, FP) and ferropervoskite ($Fe_xMg_{1-x}SiO_3$, FPv). They found that the effect of the high-spin to low-spin transition in FP caused a shift in the $10^3\ln\beta$ for $^{57}Fe/^{54}Fe$ of −0.007‰ at 4000 K and zero pressure. For reference, the effective ionic radii predict a shift of −0.076‰ for the high-spin/low-spin transition at the same temperature. One would expect ferropericlase to favor the heavy isotopes relative to ferroperovskite by virtue of the lower coordination number for iron in the former. However, the DFT calculations give the opposite result, with $10^3\ln\alpha_{FP\text{–}FPv} = -0.018$‰ at 4000 K and zero pressure using high-spin states and +0.001‰ at the same temperature and 120 GPa using low-spin and intermediate-spin for FP and FPv, respectively. The ionic model predicts a value for $10^3\ln\alpha_{FP\text{–}FPv}$ of +0.03‰ at 4000 K for high-spin states in both phases. Although crystal chemical principles are useful as guides, it is clear that at extreme conditions with complex variability in bond environments, detailed calculations and/or experiments are required to determine signs and magnitudes of relatively small equilibrium fractionation factors.

3. Three-isotope method for determining fractionation factors

Determining equilibrium isotope fractionation factors in the laboratory is challenging because of the need to demonstrate that thermodynamic equilibrium has actually been achieved. The classical experimental approach in isotope-exchange experiments is to “bracket”

equilibrium by approaching the equilibrium state from both sides in a time series where the assumption is that longer durations ensure closest approaches to equilibrium (e.g., O'Neil, 1986). Alternative experimental strategies originally developed for light stable isotopes have proven effective in recent years for non-traditional stable isotope systems at elevated temperatures. For example, Schuessler et al. (2007) augmented the classical time-series approach with the "partial exchange" method (Northrop and Clayton, 1966) to determine the equilibrium Fe isotope fractionation between pyrrhotite and silicate melts.

In recent years we have had success in deriving equilibrium isotope fractionation factors at high temperatures using the three-isotope exchange method. First introduced by Matsuhisa et al. (1978) for determining mineral-water oxygen isotope fractionation and later modified by our group at UCLA for mineral-mineral exchange of other isotope systems (e.g., Shahar et al., 2008), the thee-isotope method utilizes extrapolation to equilibrium conditions defined by three isotopes of the element of interest. The extrapolation scheme is in effect a bracketing method with the added advantage that the final equilibrium state of the system is identified precisely. We have used this method with success for the Fe, Ni, Mg and Si isotopic systems for mineral pairs (Fe, Ni, Mg), metal-silicate melt pairs (Si), and for aqueous ferric chloride complexes (Fe) (Shahar et al., 2008, 2009; Hill et al., 2010; Lazar et al., 2012; Macris et al., 2013).

With this approach the equilibrium isotope ratios of coexisting phases are obtained by extrapolation to a condition for isotopic equilibrium defined by the mass fractionation relationship between two isotope ratios in the system of interest. To see this, consider the ratio of two equations like Eq. (29), one for the ratio of isotopes 2 and 1, with mass ratio m_2/m_1, and the other for the ratio of isotopes 3 and 1, with mass ratio m_3/m_1 where $m_3 > m_2 > m_1$ (here there are two rare isotopes with masses m_3 and m_2). The result is

$$\frac{\ln\alpha_{2/1}}{\ln\alpha_{3/1}} = \frac{\left(\frac{1}{m_1}-\frac{1}{m_2}\right)}{\left(\frac{1}{m_1}-\frac{1}{m_3}\right)} = \beta. \tag{36}$$

This relationship between the two fractionation factors for the two isotope ratios can be expressed as a nearly linear curve in terms of delta values where $\delta_A^{2/1} - \delta_B^{2/1} = 10^3 \ln \alpha_{A-B,\ 2/1}$ and $\delta_A^{3/1} - \delta_B^{3/1} = 10^3 \ln \alpha_{A-B,\ 3/1}$ for equilibrium fractionation between phases A and B. The two delta values $\delta^{2/1}$ and $\delta^{3/1}$ are related through Eq. (36):

$$\delta^{2/1} = \left(10^3 + \delta^{2/1}{}_{Ref}\right)\left(\frac{10^3+\delta^{3/1}}{10^3+\delta^{3/1}_{Ref}}\right)^{\beta} - 10^3 \tag{37}$$

where subscript Ref refers to some reference isotopic composition that anchors the $\delta^{2/1}$ vs. $\delta^{3/1}$ curve in three isotope space. Eq. (37) is very nearly a straight line on a plot of $\delta^{2/1}$ vs. $\delta^{3/1}$ with slope β (not to be confused with the β in Eq. (27)) given by Eq. (36) and an intercept defined by the reference composition. It is referred to as the equilibrium fractionation line. A necessary, though not entirely sufficient, condition for isotopic equilibrium is that two phases plot on the curve (~line) defined by Eq. (37). In detail, the slope β will be slightly lower than the high-temperature approximation used here (Young et al., 2002; Cao and Liu, 2011) and the slopes are also slightly lower for kinetic isotope fractionation (Young et al., 2002). However, for most practical applications involving the rock-forming elements of interest in this context, all terrestrial materials will plot on fractionation lines in three-isotope space (i.e., $\delta_{2/1}$ vs. $\delta_{3/1}$) closely approximated by Eq. (37).

One makes use of the condition for equilibrium embodied by Eq. (37) by spiking reactants in exchange experiments with one of the isotopes of interest, displacing the material from the terrestrial fractionation line that characterizes natural materials (Fig. 7A). For Mg isotope exchange experiments, for example, one could spike one of the reactants in the experiments with the major isotope, ^{24}Mg, leading to a displacement along a line of unit slope in a plot of δ^{25}Mg vs. δ^{26}Mg (Fig. 7A). The slope-1 relationship offers convenient checks on analytical protocols. The experimental charge, usually a piston cylinder capsule of Au, graphite, or MgO, for example, will then contain materials with a bulk composition that lies between the spiked reactant and the unspiked reactant and on the slope-1 line (open circle in Fig. 7B). A series of experiments of different duration will define trajectories towards the equilibrium isotopic compositions for both reacting pairs (Fig. 7C). The intersections of these trajectories with the secondary fractionation line (SFL) defined by slope β and the bulk composition for the system give the equilibrium fractionation between the reactants (Fig. 7C). Extrapolation to the SFL is possible because the isotope exchange trajectories are indistinguishable from linear (as opposed to curved) where the system is closed to mass transfer (Lazar et al., 2012). The advantage of this approach is that equilibrium can be obtained by extrapolation where the system has not yet achieved equilibrium. Extrapolation to the SFL provides a tighter constraint on the equilibrium partitioning than bracketing alone.

Where there is loss of the element of interest to the capsule walls, spurious determinations of fractionation factors can result if the rate of diffusion into the capsule walls begins to outpace the rate of isotope exchange between reactants in the capsule. In this case, escape of the lighter isotopes to the walls by diffusion occurs faster than the exchange of isotopes within the capsule, with the consequence that the difference in isotope ratios between the reactants may not correspond to an equilibrium condition. The slope-1 initial condition relating reactants to the bulk composition of the system proves useful in identifying open-system behavior as the effective bulk drifts away from the slope-1 line (Fig. 7D). We have witnessed this open-system effect for Ni isotopes as a result of Ni alloying with Au capsules at temperatures near 950 °C (Lazar et al., 2012).

The three-isotope method was originally used for fluid–mineral systems but has now been adapted it to solid–solid reactions with success. For mineral–mineral exchange experiments, diffusion will limit the exchange of isotopes between phases. In order to circumvent this limitation, we find that the best way to achieve substantial isotope exchange is to design the experiments so that new reactants grow during the runs. For example, in the first experiments employing this method for mineral–mineral exchange by Shahar et al. (2008), iron isotope fractionation between magnetite and fayalite was investigated with a starting assemblage of hematite spiked with ^{54}Fe, fayalite, and quartz. At temperature and pressure in the piston cylinder apparatus, magnetite formed at the expense of hematite (Fig. 8), yielding the quartz–fayalite–magnetite (QFM) oxygen buffer assemblage. This strategy of forcing the growth of one of the reactants facilitates isotope exchange by dissolution and reprecipitation. Therefore, it is the rate of heterogeneous reactions vs. diffusion into capsule materials that can determine whether an experiment behave as a closed or open system (Fig. 9). Another approach, used by Macris et al. (2013), is to make use of a rapidly exchanging partner in separate experiments. In the latter case, Mg isotope exchange between forsterite and spinel was accelerated by pairing forsterite with magnesite and spinel with magnesite in parallel experiments. Isotope exchange between magnesite and either of the other two phases is accelerated by recrystallization and annealing.

Melts behave differently than solids with respect to three-isotope space. Melting of an experimental charge generally leads to homogenization prior to achieving isotopic equilibrium. The behavior would appear in Fig. 7 as a collapse of both reactants to a point corresponding to the bulk composition followed by retreat of each reactant along the SFL as they evolve from isotopically homogenized liquids. In these experiments, the advantage of extrapolating to the equilibrium compositions is lost. Nonetheless, we find that spiking one reactant is still useful as it allows one to easily assess whether the system is behaving as a closed system or an open system regardless of melting.

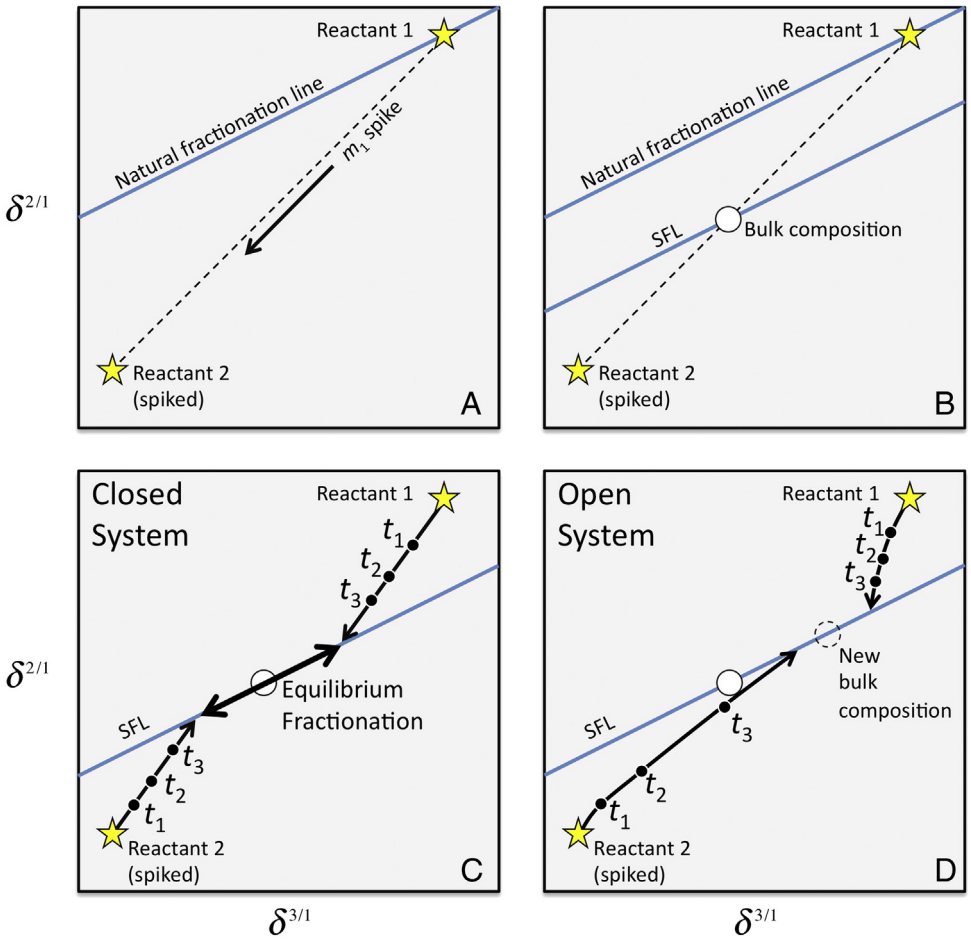

Fig. 7. Schematic showing the three-isotope method for extracting equilibrium isotope fractionation factors from isotope exchange experiments. Panel A shows the consequences of spiking one reactant with isotope 1, with mass m_1. Panel B shows the relationship between the two reactants and the bulk isotopic composition for the system and the secondary fractionation line (SFL) that passes through the bulk composition. The dashed line has a slope of unity. Panel C shows progressive equilibration exhibited by the two equilibrating phases at times t_1, t_2, and t_3 and the equilibrium fractionation factor obtained by extrapolation of the time series to the secondary fractionation line. Panel D shows the consequences of loss of the element of interest to the capsule, resulting in an open system in which the bulk composition for the two equilibrating phases has shifted, in this case to the right to higher isotope ratios.

4. Earth's mantle and crust

Equilibrium fractionation factors are the indispensible baseline for interpreting real rock data. In some cases, equilibrium can be shown to have been attained and preserved. However, this is not always the case even at high temperatures. Based on comparisons with expectations for equilibrium fractionation, persistent and recurring evidence for isotopic disequilibrium in mantle rocks has emerged recently. Examples of equilibrium and disequilibrium at high temperatures in the Fe and Mg isotopic systems are given in what follows.

4.1. Iron isotopes

Equilibrium iron isotope fractionations among minerals at high temperatures are not yet well characterized. Excluding silicate–metal fractionations described below in the section on core formation (Section 5), the only experimental data on equilibrium Fe isotope inter-mineral fractionation published to date are those of Shahar et al. (2008) for magnetite–fayalite, as described above. The remaining information comes from theory and from analyses of natural samples.

Theoretical predictions for Fe isotope fractionation have proven difficult and can lead to conflicting results, as described in the previous section (e.g., Polyakov et al., 2007; Rustad et al., 2010). However, the need for these high-temperature fractionation factors is increasing. For example, there has been considerable debate about whether or not Fe isotopes fractionate as a result of crust formation by partial melting of mantle rocks. Some have argued that such a fractionation is unlikely and others suggest it is clearly exhibited by the data (Beard and Johnson, 2004, 2007; Weyer et al., 2005, 2007; Poitrasson, 2007; Weyer and Ionov, 2007; Wang et al., 2012). This is an important issue that requires resolution before the bulk Fe isotopic composition of various solar system bodies can be determined; bulk silicate isotopic compositions relative to chondrite may allow iron isotopes to be used as monitors of planetary differentiation and core formation (Poitrasson et al., 2004; Polyakov, 2009; Williams et al., 2012; Wang et al., 2012).

Two issues pervade these debates. One is the offset, or lack thereof, between mantle rocks and basalts in Fe isotope ratios. The other is the absence of reliable fractionation factors between various minerals and between minerals and melts. Weyer and Ionov (2007) concluded that basaltic crust formation resulted in a ~ 0.1‰ increase in $^{56}Fe/^{54}Fe$. Wang et al. (2012) observed a similar enrichment of ~ 0.1‰ relative to chondrites and terrestrial peridotites in basalts from Earth, Moon, and from angrite meteorites. Dauphas et al. (2009) interpret the difference between MORB/OIB basalts and mantle peridotites as the result of fractionation caused by partitioning of incompatible Fe^{3+} to melt and Wang et al. (2012) offer a similar explanation for the angrites. However, Eqs. (29) and (31) also predict that the Fe coordination environment is important as well, and the coordination of Fe in melts can be different from that in coexisting mineral phases. The average coordination of Fe^{2+} and Fe^{3+} is approximately 5 in basaltic melts (e.g., Jackson et al., 2005; Wilke et al., 2006), while it is 6 in pyroxenes and olivine. The

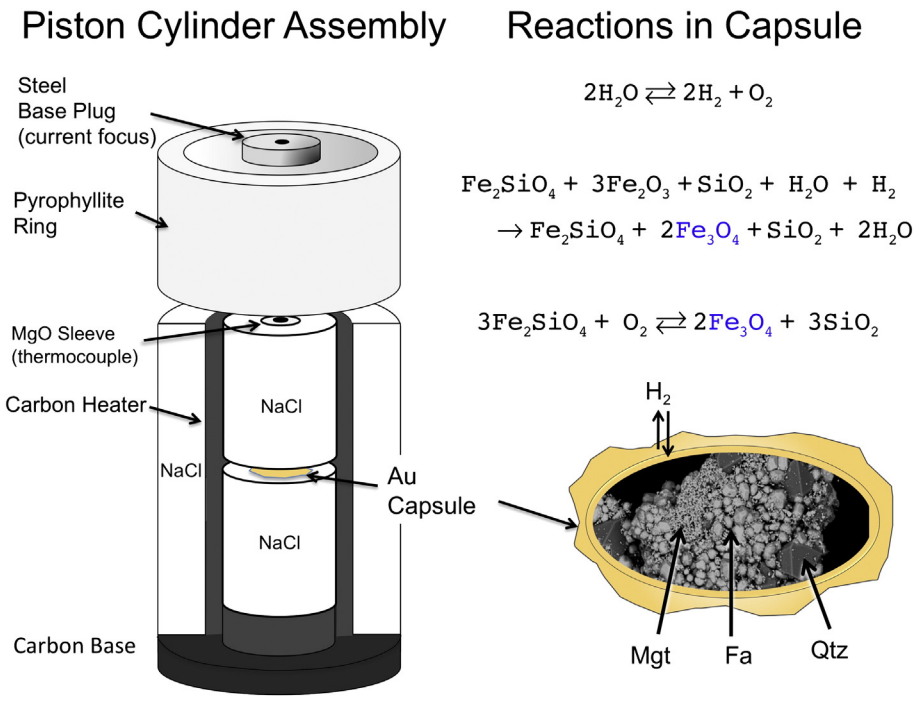

Fig. 8. Schematic of the experiment used to obtain equilibrium Fe isotope fractionation between magnetite and fayalite. The three linearly independent reactions shown describe mass transfer leading to isotope equilibrium.

lower coordination of iron in melts suggests that even in the absence of differences in oxidation state, there is a tendency for melts to concentrate the heavy isotopes of Fe. On the other hand, the lack of elevated $^{56}Fe/^{54}Fe$ in Martian basalts and in HED meteorites (crustal rocks from asteroid 4 Vesta) may be best understood in terms of the different influences of oxidation state on fractionation during igneous differentiation (Wang et al., 2012). In any case, if the estimates of fractionation with partial melting are correct, then the relatively high $^{57}Fe/^{54}Fe$ of terrestrial basalts are not evidence for a difference in iron isotopic composition between BSE and chondrite.

The iron isotope data for terrestrial mantle minerals and rocks are substantial and growing rapidly (Zhu et al., 2002; Beard and Johnson, 2004; Poitrasson et al., 2004; Williams et al., 2004, 2005, 2009; Weyer et al., 2005; Schoenberg and von Blanckenburg, 2006; Weyer and Ionov, 2007; Zhao et al., 2010, 2012). Taken as a whole the inter-mineral fractionation data vary considerably (Fig. 10). Williams et al. (2005) found significant variations in $^{57}Fe/^{54}Fe$ for a large suite of mantle rocks and their constituent minerals, resulting in some ambiguity concerning the fractionation of iron between the different phases.

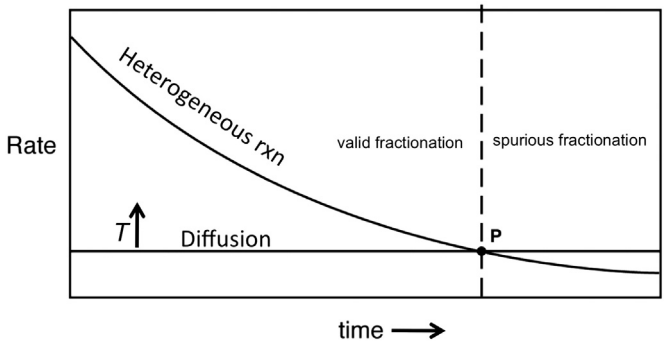

Fig. 9. Schematic illustration showing the relationship between the temperature-dependent rate of diffusion into capsule walls (up arrow signifies greater rate of diffusion with greater temperature) and rate of heterogeneous reactions driving isotope exchange. Where diffusion is faster than reaction rates, spurious results can ensue.

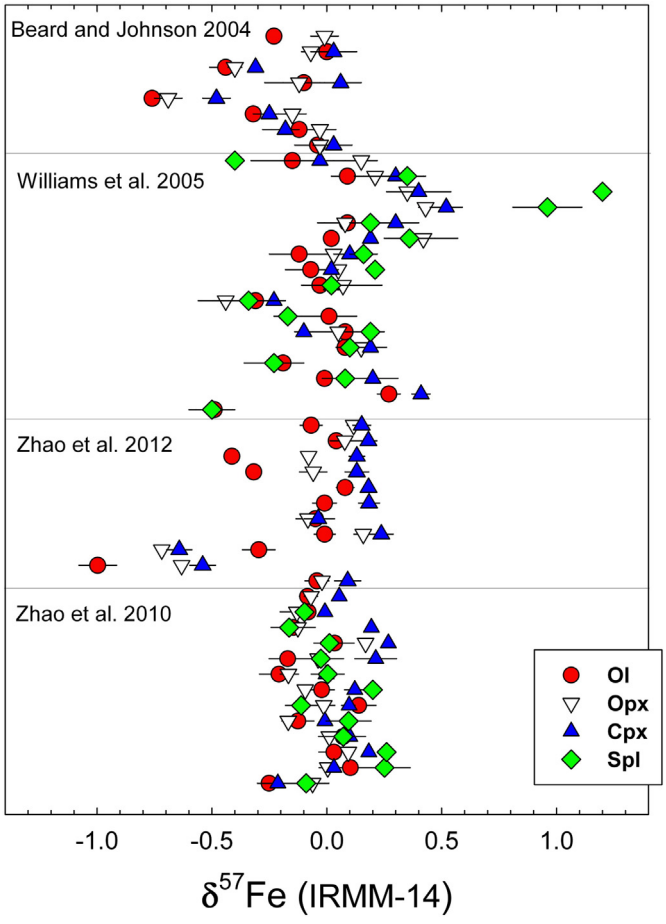

Fig. 10. Iron isotope compositions of mantle minerals. Data are from Beard and Johnson (2004); Williams et al. (2005); and Zhao et al. (2010, 2012). Ol = olivine; Opx = orthopyroxene; Cpx = clinopyroxene; Spl = spinel. Error bars represent 2 standard deviations.

For example, the study found that in some mantle rocks, spinel has greater $^{57}Fe/^{54}Fe$ than does olivine, while in others olivine exhibits the higher $^{57}Fe/^{54}Fe$ values. More recently, Zhao et al. (2010) found small but distinguishable Fe isotopic variations in spinel lherzolites and clinopyroxenites from the North China Craton. Their inter-mineral Fe isotope fractionation measurements show no clear systematics within individual xenoliths. In other words, the current inter-mineral Fe isotope fractionation data taken in aggregate show no clear trends regarding the degree of enrichment of heavy iron isotopes as a function of crystal chemistry (Fig. 10).

Even in the absence of experiments or comprehensive ab initio calculations, iron isotope fractionation factors between minerals can be estimated using crystal chemical principles in order to provide a framework for interpreting the large quantity of new measurements in rocks. For example, based on first principles (Eqs. (29) and (31)) one predicts that pyroxenes favor heavy Fe isotopes relative to olivine due to lower coordination for oxygen in the pyroxene structure (Fig. 2). Yet, in our Fe isotope study of San Carlos mantle xenoliths (Macris et al., 2015) we have found the reverse, with many pyroxenes exhibiting lower $\delta^{57}Fe$ ($\delta^{57}Fe$ refers to the per mil deviation in $^{57}Fe/^{54}Fe$ from the IRMM-14 standard) than olivine as seen in δ–δ plots (Fig. 11). This constitutes evidence for disequilibrium involving pyroxenes and is consistent with earlier observations in mantle xenoliths based on rare earth elements (Frey and Prinz, 1978) and lithium isotopes (Jeffcoate et al., 2007) that pyroxenes are selectively affected by reactions with partial melts or fluids (metasomatism). Conversely, spinel is observed to have greater $^{57}Fe/^{54}Fe$ than coexisting olivine as expected from first principles, providing no evidence for open-system behavior on δ–δ plots (Fig. 11).

Calculations using Eqs. (29) and (31) suggest that spinel should indeed concentrate the heavy isotopes of iron relative to olivine and pyroxenes. However, modeling of the kinetic energy associated with Fe vibrations using Mössbauer second-order Doppler shift data suggests that spinel should favor light Fe isotopes relative to olivine (Polyakov, 1997; Polyakov and Mineev, 2000), a prediction that is diametrically opposed to conclusions from simple crystal chemical arguments. Revisions to the Mössbauer-derived fractionation factors based on kinetic energies derived from NRIXS data (Polyakov et al., 2007) raise doubts about this earlier prediction.

These opposing predictions, combined with the variability seen so far in natural samples, raises important questions about Fe isotopes in the mantle. What is the temperature-dependent equilibrium Fe isotope fractionation between spinel and silicates? Can these fractionation factors be used to interpret the complex and often conflicting inter-mineral Fe isotope data?

The need for a better understanding of equilibrium iron isotope fractionation factors is of course not limited to spinel–silicate pairs in the mantle. For example, Telus et al. (2012) have argued for equilibrium Fe isotope fractionation factors relevant to more silicic igneous systems. Williams et al. (2009) showed recently that there is a positive correlation between $\delta^{18}O$ and $\delta^{57}Fe$ in a suite of eclogitic xenoliths that cannot be explained by inheritance from oceanic crust. Instead these authors suggest that this correlation is a product of fractional melting with garnet as an important residue phase. The Williams et al. Fe isotope data include garnets with lower $\delta^{57}Fe$ than coexisting clinopyroxenes and correlation between $\delta^{57}Fe_{Grt}$ and $\delta^{57}Fe_{Cpx}$ (Fig. 4) implying an equilibrium pyroxene-garnet $^{57}Fe/^{54}Fe$ fractionation of ~ 0.4‰. Here again, the relative enrichment of the heavy Fe isotopes between these two phases is generally consistent with expectations, as described in the previous section. Pyroxene/garnet Fe isotope fractionation was used as a model for melt-residue fractionation in the work by Williams et al., but accurate equilibrium fractionation factors are required for more quantitative modeling.

Attempts to improve on this situation from the viewpoint of theoretical predictions from NRIXS data were presented recently by Dauphas et al. (2012). We note, however, that our experimental calibration of the magnetite–fayalite Fe isotope fractionation factor is significantly different from several theoretical predictions (Shahar et al., 2008), underscoring the need for experimental calibrations wherever possible.

4.2. Magnesium isotopes

Recent work on the Mg isotopic compositions of mantle minerals and rocks (Wiechert and Halliday, 2007; Handler et al., 2009; Young et al., 2009; Bourdon et al., 2010; Chakrabati and Jacobsen, 2010; Liu et al., 2011; Pogge von Strandmann et al., 2011; Teng et al., 2013; Xiao et al., 2013) suggests that, as with the isotopes of iron, magnesium experiences open-system isotopic exchange between reservoirs in the mantle. An understanding of the sources of the consequent variations in $^{25}Mg/^{24}Mg$ and $^{26}Mg/^{24}Mg$ is required for assessing the Earth's bulk Mg isotopic composition with implications for the processes attending the formation of the planet (e.g., fractionation attending sublimation and evaporation before and during planet formation). Young et al. (2009) found that while clinopyroxene $^{25}Mg/^{24}Mg$ was of order

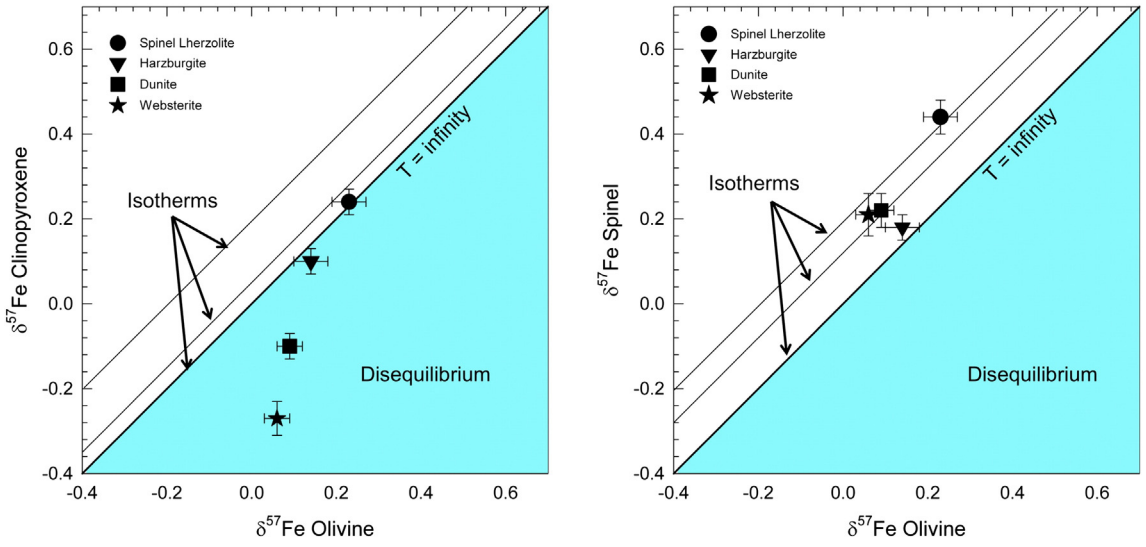

Fig. 11. $\delta^{57}Fe$–$\delta^{57}Fe$ plots showing clinopyroxene–olivine disequilibrium (beyond maximum temperature) where for equilibrium $\delta^{57}Fe_{CPX} > \delta^{57}Fe_{Oliv}$ and probable spinel–olivine equilibrium assuming $\delta^{57}Fe_{Spl} > \delta^{57}Fe_{Oliv}$ at equilibrium (after Macris et al., 2015). Shaded regions are where the sign of the apparent fractionation is opposite to that expected for equilibrium. Data are reported relative to the IRMM-14 Fe isotope standard.

0.15‰ greater than predictions for equilibrium with olivine would suggest, this metasomatic effect altered the whole-rock xenolith $^{25}Mg/^{24}Mg$ by no more than 0.02‰. Therefore, based on comparisons with analyses of chondrites, Young et al. (2009) were able to conclude that bulk silicate Earth has a $^{25}Mg/^{24}Mg$ that is + 0.05 +/− ~0.03‰ relative to chondrites. A value of + 0.04 +/− 0.06 was later obtained by Pogge von Strandmann et al. (2011) based on whole-rock measurements of chondrites and mantle xenoliths. Although not all laboratories yet agree, with some showing larger differences and others no resolvable difference at all (e.g., Bourdon et al., 2010), our view is that there is ample evidence for a slight difference between BSE and chondrite in magnesium isotope ratios. A key to such assertions is accounting for open-system effects identified by deviations from isotopic equilibrium. The reason behind this difference between BSE and chondrite, if proven to be robust, is uncertain but potentially profound.

In our initial work on San Carlos mantle minerals (Young et al., 2009) we pointed out that the largest inter-mineral fractionation in the Mg isotopic system in many mantle xenoliths is between spinel and olivine. The observation that δ^{25}Mg spinel > δ^{25}Mg pyroxene > δ^{25}Mg 25Mg olivine is consistent with our understanding of the bonding environment of Mg in these minerals and our data match expectations from theory (δ^{25}Mg refers to the per mil deviation in $^{25}Mg/^{24}Mg$ from a standard, in this case DSM3). Nonetheless, Young et al. found that in detail, pyroxenes were seemingly out of Mg isotopic equilibrium with both olivine and spinel, and this has been observed subsequently by several groups (Pogge von Strandmann et al., 2011; Xiao et al., 2013). These authors all attributed this effect to metasomatism involving pyroxene but not olivine or spinel (as in the case of Fe isotopes for these rocks). Involvement of a major rock-forming element like Mg in metasomatism is an important constraint on the reactive agents (melts and/or fluids) and physical conditions attending new mineral growth (e.g., clinopyroxene replacement of orthopyroxene).

In addition Young et al. found that the temperature indicated by the spinel-olivine Mg isotope fractionation, using fractionation factors obtained by density functional theory calculations (Schauble, 2011), is consistent with the temperature obtained from ordering parameters in spinel for similar rocks (about 820 °C). They took this as indication that spinel and olivine are indeed in Mg isotopic equilibrium and that the theoretical estimates for the fractionation factors are about right.

However, Liu et al. (2011) found both pyroxene–olivine and spinel–olivine Mg isotope fractionations in xenoliths correlate with $1/T^2$, where temperatures are derived in this case from two-pyroxene cation thermometry rather than from ordering parameters. From these data Liu et al. concluded that all xenolith phases are in Mg isotopic equilibrium at the temperatures recorded by cation exchange, implying that Mg was not mobile. This conclusion contrasts with that of Young et al. (2009), Pogge von Strandmann et al. (2011) and Xiao et al. (2013) and would suggest that metasomatism involving melts that often affect the chemistry and lithium isotopes in pyroxenes (Rudnick and Ionov, 2007; Pogge von Strandmann et al., 2011) did not affect Mg isotope in these rocks. Liu et al. also find smaller spinel–olivine fractionations in mantle xenoliths than those found by Young et al. (2009) by several tenths of per mil even when correcting for differences in equilibration temperatures.

The effects of mineral chemistry on fractionation are crucial to all interpretations of Mg isotope data at high temperature. Liu et al. attribute the lower spinel–olivine Mg isotope fractionation values relative to those of Young et al. mainly to the effects of octahedral-site cation substitutions in spinel (Cr and Fe^{3+} for Al) that are typical of the xenoliths. Their suggestion is based on calculations by Schauble (2011) showing that substitution of Cr and/or Fe^{3+} for Al lengthens Mg–O bonds, reducing bond strength and lowering the affinity for ^{26}Mg over ^{24}Mg relative to $MgAl_2O_4$-spinel by ~0.7‰ at 1000 K (Fig. 12). However, cation substitution in spinel does not, by itself, explain the relatively small differences in δ^{26}Mg between spinel and olivine, as discussed below.

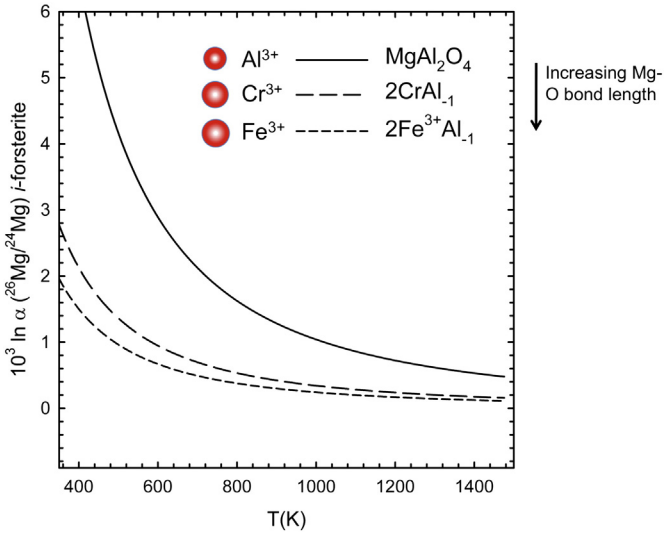

Fig. 12. Predicted spinel–olivine $^{26}Mg/^{24}Mg$ fractionation as a function of spinel octahedral site occupation (after Schauble, 2011). Substitution of Cr or Fe^{3+} for Al lengthens the Mg–O bond, reducing bond strength. The *i* on the ordinate label indicates that the fractionation factors are for different spinel compositions.

The examples above demonstrate the need for accurate calibrations of fractionations if the meaning of inter-phase variations in δ^{26}Mg are to be interpretable. Macris et al. (2013) used the three-isotope method to calibrate the spinel–forsterite Mg isotope fractionation factor as a function of temperature (Fig. 13). These results are compared with the theoretical predictions (Schauble, 2011) and the data from Young et al. (2009) and Liu et al. (2011) in Fig. 13.

There is excellent agreement between our experiments and the ab initio predictions. The data in turn confirm that San Carlos xenolith spinel–olivine fractionations observed by Young et al. (2009) are consistent with spinel ordering temperatures based on fractionation factors for pure $MgAl_2O_4$. The experimental results also confirm that the Liu

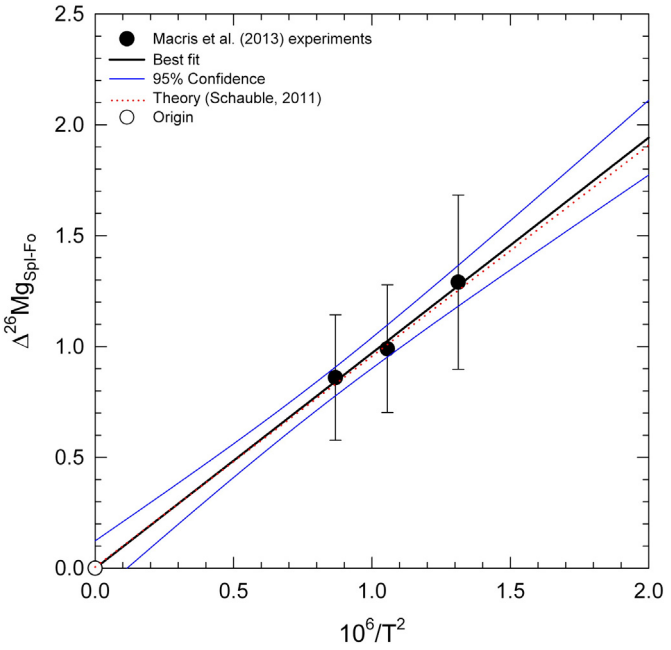

Fig. 13. Experimental calibration of the $^{26}Mg/^{24}Mg$ fractionation factor between $MgAl_2O_4$ spinel and forsterite olivine obtained at UCLA (re-plotted from Macris et al., 2013). Regression includes the origin. The error envelope in this plot includes a nominal uncertainty in the origin. Also shown is the prediction from density functional perturbation theory by Schauble (2011).

et al. (2011) data are indeed inconsistent with pure $MgAl_2O_4$ spinel–olivine fractionation. Fig. 14 shows the spinel–olivine fractionation factor obtained by linear mixing of the end-member β factors for spinel to obtain a fractionation factor for the typical spinel compositions in the xenoliths. The mismatch between this calculated fractionation and the data indicates that theoretical predictions for the effects of $CrAl_{-1}$ and $Fe^{3+}Al_{-1}$ in mantle spinels do not explain the Liu et al. data quantitatively.

We conclude that further experiments are required in order to calibrate the effects of cation substitution on spinel–forsterite Mg isotope fractionation factors. Without these data it is not possible to establish unequivocally whether or not observed inter-mineral Mg isotope fractionations represent equilibrium or disequilibrium. Conversely, with calibrations for the effects of cation substitutions, spinel–olivine magnesium isotope fractionation should prove to be a sensitive tracer of mantle metasomatism and/or equilibration temperatures.

5. Isotope fractionation and core formation

The concept of using stable isotope ratios as proxies for the abundances of light elements in the core began in earnest with the paper by Georg et al. (2007) for silicon. The concept is straightforward. Isotope partitioning between Fe–Ni metal and silicate can cause a difference in isotopic composition between bulk silicate Earth and bulk Earth, the latter usually being assumed to be similar to chondrite meteorites. The general scheme in the case of Si is outlined in Fig. 15 in which the relationship between the oxygen fugacity, temperature and pressure-dependent partitioning of Si between metal and silicate (i.e., core and bulk silicate Earth) is related to the offset in $^{30}Si/^{28}Si$ between bulk silicate Earth and bulk Earth (the latter assumed to be chondritic).

5.1. Silicon in the core

The key parameter in assessing the isotopic consequences of Si partitioning between core and mantle is the isotope fractionation factor. Initial estimates from theory indicated that the heavy isotopes of Si are concentrated in silicate relative to Si-bearing Fe metal at equilibrium (Georg et al., 2007). However, the Fe–Si bonding characteristics of iron

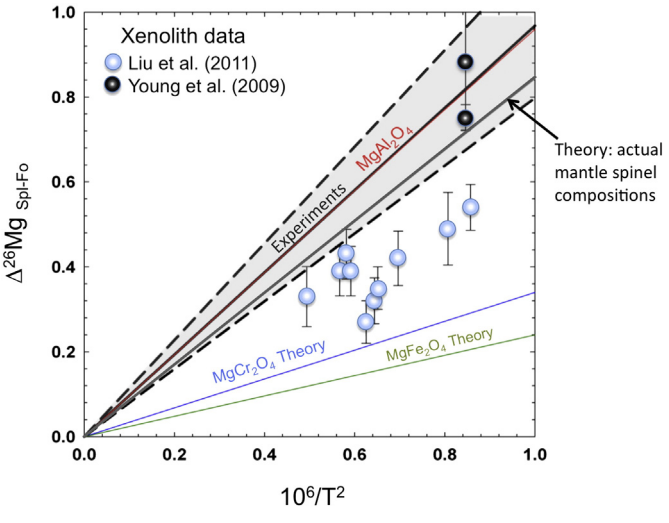

Fig. 14. Comparison of experimentally-derived spinel–forsterite $^{26}Mg/^{24}Mg$ fractionation factor (heavy black line) with uncertainties (dashed lines) and data for mantle xenoliths by Young et al. and Liu et al. (solid symbols). Also shown are calculated fractionation factors vs. temperature and composition (after Schauble, 2011). The predicted $MgAl_2O_4$–forsterite fractionation, in red, is hidden behind the experimental black line. Gray line labeled "Theory: actual mantle spinel compositions" represents the predicted spinel–forsterite fractionation for the typical mantle xenolith spinel composition used by Liu et al. (2011). Figure modified after Macris et al. (2013).

silicide is a subject for intensive study and a truly quantitative measure of the Si isotope fractionation factor between Fe-rich metal and mantle-like silicates requires measurements in real materials, either in the laboratory or in equilibrated rocks, or both.

Experimental determinations of the Si isotope fractionation factor between molten silicate (~pyrolite) and molten metal as a function of temperature at 1 GPa in graphite capsules were obtained by Shahar et al. (2009). This work was followed up with a study at 7 GPa in MgO capsules by Shahar et al. (2011). Both studies are the products of experiments conducted at the Geophysical Laboratory and Si isotope ratio data obtained by acid digestions and by laser ablation at UCLA and give consistent results within uncertainties (Fig. 16). Remarkably, a study of Si isotope fractionation between enstatite and Si in coexisting Fe metal in two equilibrated enstatite achondrite meteorites (aubrites) by Ziegler et al. (2010), again obtained both by acid digestion and by laser ablation at UCLA, gives the same temperature-dependent fractionation relationship (Fig. 16). The temperature-dependence defined by these two sets of experiments and the meteorite data follows the expected T^{-2} functional form. Ab initio calculations comparing solid forsterite olivine and Fe_3Si by Schauble (reported in Ziegler et al., 2010) predict a silicate–metal fractionation factor that is ~ 12% lower than the experimental values (Fig. 16). Most recently, Hin et al. (2014) reported experiments between molten basaltic silicate and metal that yields a silicate–metal Si isotope fractionation factor ~ 40% lower than the previous experimental and meteoritical data. Our view at present is that the agreement between two different sets of experiments in two distinct capsule materials at different conditions, meteorite data that are entirely independent of experimental procedures, and two types of analytical approaches (acid digestion and laser ablation) makes it highly unlikely that the UCLA/Geophysical laboratory work can be giving erroneous estimates of $\Delta^{30}Si_{Silicate-metal}$ by as much as 2‰ in the case of the meteorites, and 1‰ in the case of the experiments. Furthermore, these hypothesized erroneous values would have to follow the T^{-2} relationship as well, making disequilibrium or spurious analytical results all the more unlikely. Therefore, we conclude that the difference between the three earlier studies and that of Hin et al. is at present unexplained but may be related to open-system effects in longer experimental runs in the Hin et al. study or the presence of abundant Sn in the metal phase in the lower-temperature runs in that study (a 0.4‰ greater fractionation reported for the longest-duration Sn-free high-T datum is in agreement with the UCLA data in Fig. 16).

Some perspective is warranted at this juncture. One suspects that approximately a decade ago, few workers in the field would have guessed that the Si isotope fractionation between silicate and metal would be several per mil at thousands of kelvins (Fig. 16). That it is so tells us something fundamental about the pliable nature of the Si–Fe bond compared with Si–O bonds, presumably due to the delocalization of charge associated with reduction of the Si atoms. It also tells us that high-temperature equilibrium fractionation can be much larger than our first instincts would dictate.

With confidence in the $\Delta^{30}Si_{Silicate-metal}$ vs. T relationship, the meaning of the apparent difference between $\delta^{30}Si$ values in BSE and in chondrites (representing bulk Earth) can be assessed quantitatively. The difference depends on the conditions attending core formation. Conditions for metal–silicate equilibration during core formation have been estimated to be ~ 40 GPa and ~ 3000 K based on moderately siderophile trace element partitioning (Zerr et al., 1998; Wood, 2008). Oxygen fugacity during core formation is less well constrained but could have been lower than the present-day mantle value of IW − 1 by a log unit or so (using non-ideal activity models) (Wade and Wood, 2005). Oxygen fugacity affects the expected difference in $\delta^{30}Si$ values between BSE and chondrite by affecting the fraction of Si in the core (Fig. 15).

One of the principal characteristics of the core is the 10% density deficit thought to be indicative of light elements there (Birch, 1964). A Si concentration of ~ 6 +/− 1 wt.% in the core would shift the bulk

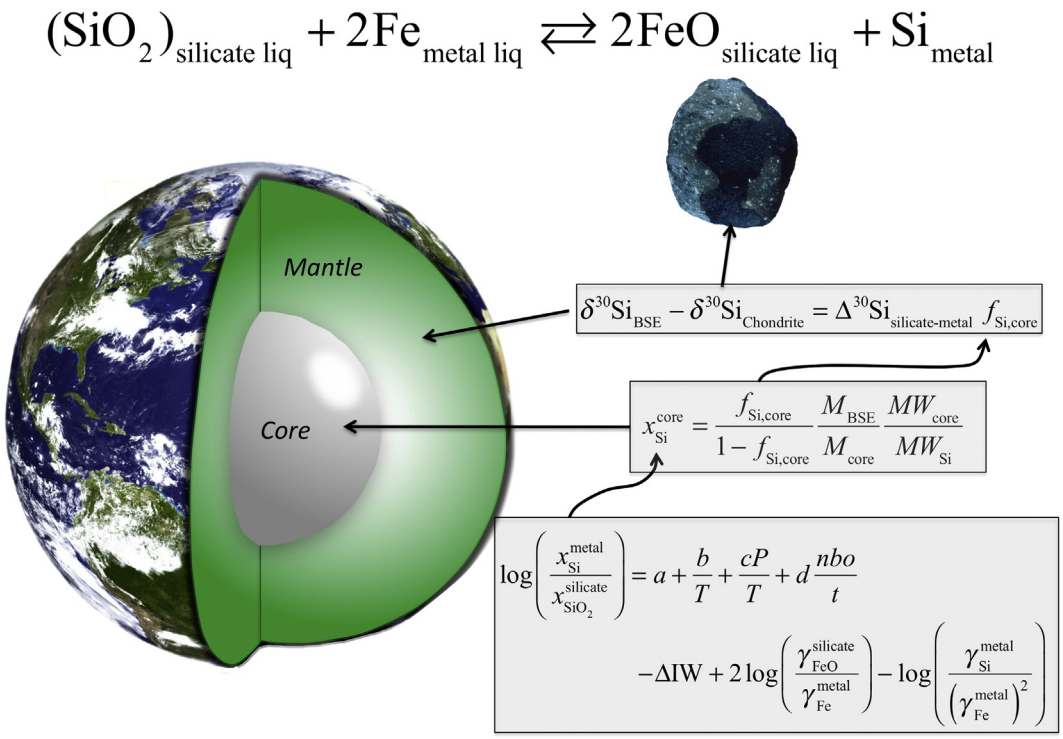

Fig. 15. Schematic illustrating the connection between the difference in silicon isotope ratios ($\delta^{30}Si$) between bulk silicate Earth (BSE) and chondrite (inset), and the fraction of Si in Earth's core prescribed by the oxidation state of equilibration (ΔIW) assuming the bulk Earth is chondritic in Si isotope ratios. In the equations $f_{Si,\ core}$ is the fraction of Earth's silicon in the core, x_{Si}^{metal} is the mole fraction of Si in metal (in this case the core), $x_{SiO_2}^{silicate}$ is the mole fraction of silica in the silicate Earth, and γ_i^j values refer to activity coefficients for the species i in phase j indicated. Parameters a, b, and c correspond to entropy, enthalpy, and volume reaction parameters while nbo/t refers to the ratio of non-bridging oxygens to tetrahedrally-coordinated cations in the silicate melt as described by Corgne et al. (2008).

Earth Mg/Si to chondritic (in the vicinity of values for CV and CI chondrites, for example) and away from the supra-chondritic BSE value and would account for some of the density deficit in the core. A value of 18 wt.% would explain the total 10% density deficit of the core but is unlikely as Si is not the only light element that may partition to metal. Fig. 17 shows contours of $\Delta^{30}Si_{BSE\text{-}bulk\ Earth} = \delta^{30}Si_{BSE} - \delta^{30}Si_{bulk\ Earth}$ as a function of temperature and pressure along the planet adiabat and ΔIW, the oxygen fugacity of equilibration in terms of log-unit deviations from the IW oxygen fugacity buffer. The quantitative relationships lead to some robust conclusions. For example, the 6 wt.% Si in

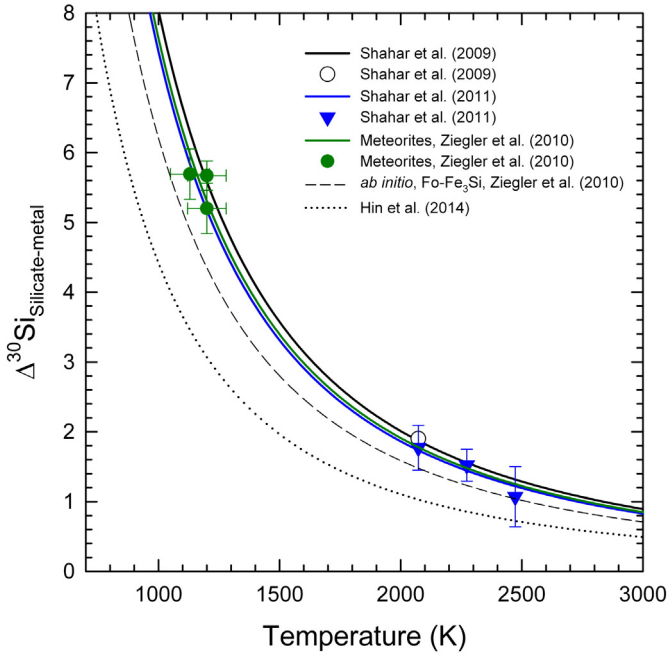

Fig. 16. Summary of temperature-dependent Si isotope fractionation between mantle-relevant silicates and Si-bearing Fe metal in the laboratory and in equilibrated meteorites. Data are from Shahar et al. (2009) in C capsules, Shahar et al. (2011) in C and MgO capsules, and Ziegler et al. (2010) from the Mt. Egerton and Norton County meteorites. Also shown for comparison are experiments from Hin et al. (2014) and ab initio calculations for olivine–Fe_3Si.

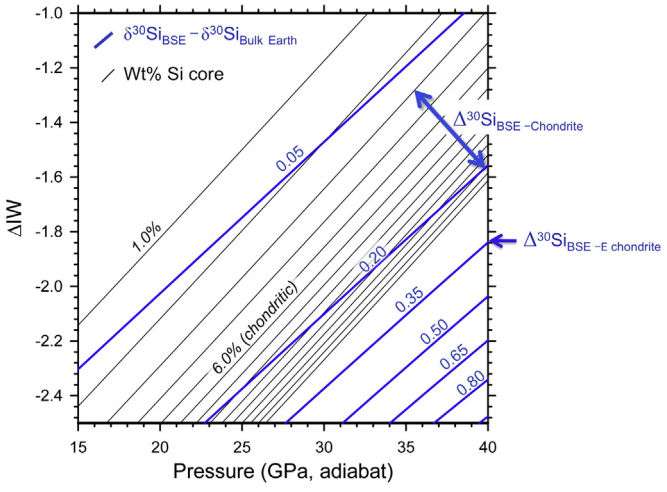

Fig. 17. Contours for weight per cent Si in Fe metal (black lines, representing Earth's core) and difference in $\delta^{30}Si$ in bulk silicate Earth (BSE) vs. bulk Earth (blue lines) as functions of oxygen fugacity (ordinate), expressed as the departure from the Iron (Fe)–Wüstite (FeO) oxygen buffer in log units (ΔIW), and pressure and temperature along the terrestrial adiabat (abscissa). The contour interval for wt.% Si in metal is 1%. Range of published differences in $\delta^{30}Si$ between BSE and ordinary and carbonaceous chondrites, the latter representing bulk Earth, is shown with the double arrow. The difference between BSE and enstatite chondrite of ~ 0.35‰ is also indicated.

the core that would be consistent with a chondritic Mg/Si for Earth is consistent with the range in measured values for $\Delta^{30}Si_{BSE-chondrite} = \Delta^{30}Si_{BSE-bulk\ Earth}$ (Savage et al., 2014) over a large range of temperatures, pressures, and oxygen fugacities. Conversely, an Enstatite chondrite Earth is seemingly ruled out for all conditions because equating $\Delta^{30}Si_{BSE-E-chondrite}$ with $\Delta^{30}Si_{BSE-bulk\ Earth}$ makes the latter so large that the required amount of Si in the core would far exceed the 10% density deficit, as pointed out previously by Fitoussi and Bourdon (2012).

In addition, assuming equilibration at 40 GPa (and approximately 3000 K), the maximum $\Delta^{30}Si_{BSE-chondrite}$ requires core formation at an oxygen fugacity approximately one half log unit below the present-day upper mantle. The lower end of the range of $\Delta^{30}Si_{BSE-chondrite}$ values requires no change in oxygen fugacity between core formation and today. At present, the limiting parameter for constraining the conditions for core formation using Si isotope ratios is not the fractionation factor, but rather the uncertainty in $\Delta^{30}Si_{BSE-bulk\ Earth}$ caused by disagreement about the "typical" $^{30}Si/^{28}Si$ of chondrites and the inevitable uncertainty as to whether bulk Earth is truly chondritic in this isotope ratio.

5.2. Fe isotope fractionation with core formation

There may be an Fe isotopic signature of core formation in the bulk silicate Earth. Continuing our theme of using first principles to guide our intuition, we note that bonds with delocalized electrons are shorter, and therefore stiffer, than bonds with localized electrons (Shannon, 1976). In effect, itinerant electrons in the Fe metal structure permit nuclei to fit together more tightly. Therefore, the expectation is that heavy iron isotopes should favor the stiffer metallic bonds in metal relative to the Fe–O bonds in silicates. Results from experiments are mixed. Poitrasson et al. (2009) found no statistically resolvable fractionation between molten metals and silicates, although uncertainties in the data are too large compared with the expected fractionations at the temperatures of the experiments. Hin et al. (2012) also found no fractionation between molten metal and silicate. However, Shahar et al. (2014) identified a significant fractionation between martian and terrestrial analog silicate melts and Fe–Ni–S alloys at 1923 K. Computational predictions for iron metal–sulfide (troilite) and iron metal–enstatite iron isotope fractionations (Polyakov and Mineev, 2000; Polyakov et al., 2007) suggest that the fractionation between sulfide and silicate is very much smaller than between either phase and metal; i.e., $\Delta^{57}Fe_{Metal-sulfide} \sim \Delta^{57}Fe_{Metal-silicate} >> \Delta^{57}Fe_{Silicate-sulfide}$. They suggest further that a fractionation of order 0.1‰ at 2000 K is to be expected, consistent with the results of both Shahar et al. (2014) and Poitrasson et al. (2009) (though the latter concluded that their data were indicative of no fractionation at the time due to the uncertainties). The various results for Fe isotope fractionation between sulfur-absent metal and silicate or sulfide are summarized in Fig. 18.

Some preliminary work on Fe isotope fractionation between sulfides + silicate and metal in the Norton County enstatite achondrite meteorite (Jordan and Young, 2014) (one of the same samples used in the Si study by the UCLA group) yields a fractionation consistent with the S-free experimental results obtained by Shahar et al. (2014) and with theoretical predictions (Polyakov and Mineev, 2000; Polyakov et al., 2007). We conclude that, as is the case for Si isotope fractionation between metal and silicate, there is a sizable fractionation of Fe isotopes between metal and silicate and that equilibrated meteorite samples are in agreement with at least some experimental results.

At face value the relatively small Fe isotope metal/silicate fractionation compared with that for Si leads to the prediction of a significantly smaller $\Delta^{57}Fe_{BSE-chondrite} = \Delta^{57}Fe_{BSE-bulk\ Earth}$ of 0.02‰ for a core–mantle equilibration temperature of 3000 K. This is at, or just below, current detection limits, perhaps explaining why there is evidently no clear difference in $\delta^{57}Fe$ between BSE and chondrites after correction for igneous differentiation (see Section 4.1). However, the metal–silicate fractionation factors determined thus far at low pressures are likely not applicable to Earth's core formation and instead may be most applicable to smaller solar system bodies like Vesta.

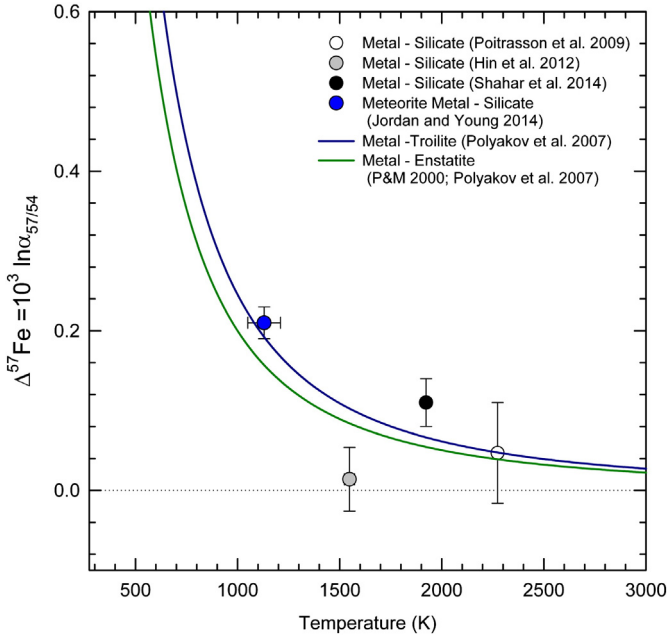

Fig. 18. Metal–silicate or metal–sulfide $^{57}Fe/^{54}Fe$ fractionation factors as functions of temperature as determined by experimental studies, theory, and a preliminary result for the Norton County enstatite achondrite (Jordan and Young, 2014). P&M 2000 refers to Polyakov and Mineev (2000).

A complicating factor for the application of the metal–silicate fractionation factors to bodies the size of Earth is the evidence for a pronounced pressure effect on the fractionation that includes a change in sign. At lower-mantle conditions, the Fe isotope fractionation between metal and Fe^{2+} in silicate and oxide, $\Delta^{57}Fe_{Metal-rock}$, is predicted to change from positive to negative, yielding $\Delta^{57}Fe_{Metal-rock} \sim -0.13$ at 2000 K (Polyakov, 2009). The change in sign apparently occurs at ~ 100 GPa (Polyakov, 2009). Experimental evidence for negative $\Delta^{57}Fe_{Metal-rock}$ values at somewhat lower pressures was obtained by Williams et al. (2012). These authors used the three-isotope exchange method to document $\delta^{57}Fe$ in aluminous Fe^{3+}-bearing silicate perovskite greater than that for coexisting iron metal by at least ~1.35‰ at 2120 K and 24 GPa. The large value for $\delta^{57}Fe$ in the silicate perovskite relative to metal is apparently due to the presence of Fe^{3+} in the silicate. The degree to which lower-mantle disproportionation reactions ($2Fe^{2+} \rightarrow Fe^{0} + Fe^{3+}$), which influence rock–metal fractionation by enhancing the Fe^{3+} component in silicates and oxides, contribute to core-mantle iron isotope fractionation depends on the details of the core-forming process. At present, the evidence from moderately siderophile trace element data suggesting equilibration pressures of ~ 40 GPa is consistent with the possibility of high $^{57}Fe/^{54}Fe$ in the Earth's mantle due to core formation as described by Williams et al. Transitions from high-spin to low-spin in Fe at pressures of ~ > 80 GPa also enhance the propensity of heavy Fe isotopes to concentrate in rock relative to metal, as described in greater detail in Section 2.4, and is relevant to core formation if material was excavated from the deep mantle during equilibration. In all cases, the veracity of the argument that Earth's mantle records an Fe isotope effect due to core formation depends critically on estimates of the $^{57}Fe/^{54}Fe$ of BSE. Williams et al. (2012) argue that by comparing basalts from different solar system bodies, representing similar degrees of partial melting, it is clear that $\delta^{57}Fe$ of BSE is greater than bulk silicate from these other bodies. Dauphas et al. (2009), on the other hand, find no evidence for a difference between BSE and chondrite $^{57}Fe/^{54}Fe$ values. If all rocky bodies in the solar system have chondritic bulk $^{57}Fe/^{54}Fe$, both conclusions cannot be true. The resolution of these apparently conflicting

observations will require a detailed understanding of the Fe isotope fractionation attending partial melting. The finding that angrites, rocks from a small asteroid-sized parent body, have δ^{57}Fe values similar to terrestrial and lunar basalts (Wang et al., 2012) would seem to contravene the hypothesis of Williams et al. (2012) that only larger bodies with sufficient pressure for ferrous iron disproportionation (~Earth-sized or larger) would produce basalt with high δ^{57}Fe values relative to chondrite.

5.3. Other isotopic consequences of core formation

Other elements of interest for core formation from an isotopic perspective include, but are not limited to, hydrogen, oxygen, and nickel (although H and O are not "non-traditional" they are of interest in view of the results for Si). No definitive work has been conducted thus far on isotopic fractionation between metal and silicate for hydrogen and oxygen. However, one can garner crude estimates of the effects from existing data.

For example, in the case of D/H, one can estimate $10^3 \ln \alpha_{\text{Silicate–metal, D/H}}$ from the sum $10^3 \ln\alpha_{\text{Silicate–H}_2\text{O,D/H}} + 10^3 \ln \alpha_{\text{H}_2\text{O–H}_2\text{,D/H}} + 10^3 \ln\alpha_{\text{H}_2\text{–metal,D/H}}$. The last term was modeled by Schauble (unpub.), yielding $10^3 \ln\alpha_{\text{H}_2\text{–FeH, D/H}} \sim 3.26/T^2$. The silicate–$H_2O$ term can be equated with silicate melt–H_2O fractionation from Kuroda et al. (1982), and the H_2O–H_2 fractionation can be obtained from Richet et al. (1977). The result is $\Delta D_{\text{Silicate–metal}} = 10^3 \ln \alpha_{\text{Silicate–metal, D/H}} \sim 4.5 \times 10^8/T^2$. At 3000 K the implied fractionation between silicate and Fe metal is ~ 50‰. Using the H content of the core estimated by extrapolation of elemental condensation temperatures by McDonough (2003), and assuming two oceans worth of water in the mantle, one arrives at a value of 0.69 for the fraction of Earth's total hydrogen resident in the core. Using the simple conservation expression $\delta D_{\text{Bulk Earth}} = (\delta D_{\text{BSE}} - \Delta D_{\text{Silicate-metal}})\ 0.69 + (1 - 0.69)\ \delta D_{\text{BSE}}$ we obtain a value of −35‰ for the difference between bulk Earth and bulk silicate Earth, $\delta D_{\text{Bulk Earth}} - \delta D_{\text{BSE}} = -35$, at 3000 K; the core could contain a reservoir of isotopically light hydrogen sufficient to increase the BSE D/H by 35‰. Given the uncertainties involved, including the ambiguity in assignment of a single D/H for chondrites to represent bulk Earth, this difference between bulk Earth and bulk silicate Earth is not detectable at present.

In the case of $^{18}O/^{16}O$ we may use silicon as a guide. Silicon isotope fractionation between silicate and metal is dominated by $10^3 \ln\beta$ of the former. In effect, $10^3 \ln\beta$ for Si in Fe metal is negligible compared with the values for silicates. If the same is true for oxygen, the $10^3 \ln\beta$ for $^{18}O/^{16}O$ in enstatite suggests a silicate-metal fractionation of ~ 0.9‰ at 3000 K (Méheut et al., 2009). The reservoir effect would be similar to that for Si in that the bulk of Earth's oxygen, even with a few weight per cent oxygen in the core, still resides mainly in the mantle. Therefore, accounting for the small leverage that the core would have for shifting the isotopic composition of the mantle, we expect a few tenths of per mil difference between bulk Earth and bulk silicate Earth at most for a batch equilibration during core formation. The difficulty is that we don't know how to assign a bulk Earth (as opposed to a BSE) $^{18}O/^{16}O$ to this level of precision.

The case for Ni is on firmer experimental ground. Lazar et al. (2012) used the three-isotope exchange method to measure the equilibrium $^{62}Ni/^{58}Ni$ fractionation between Ni metal and Ni-talc at low pressures. They found that like iron, the heavy Ni isotopes are concentrated in the metal relative to the silicate. The result is qualitatively consistent with the L5 Ausson meteorite data in which metal was found to be higher in $^{62}Ni/^{58}Ni$ than coexisting chondrule material. Using the derived temperature-dependent fractionation, the silicate-metal $^{62}Ni/^{58}Ni$ fractionation at 3000 K is −0.03‰ (δ^{62}Ni silicate < δ^{62}Ni metal by 0.03‰). With ~90% of Earth's Ni in the core, the difference between bulk Earth and BSE δ^{62}Ni should be < 0.03‰ for a single-stage of equilibration during core formation. Identifying such a small difference between average chondrite (representing bulk Earth) and mantle materials will be challenging for the near future. Lazar et al. point out that a Rayleigh distillation of Ni into the core could raise the difference between bulk Earth (chondrite) and BSE to as high as 0.1‰. Of course these data were obtained at low pressures and estimates for lower mantle conditions, from both experiments and theory, are warranted.

6. Concluding remarks

The last decade has witnessed a veritable explosion of "non-traditional" stable isotope ratio data for the rock-forming elements. The increase in the volume of non-traditional stable isotope data from natural samples will be of limited value without commensurate improvements in our understanding of the factors controlling equilibrium stable isotope fractionation as a baseline for our interpretations. Throughout this review we have tried to illustrate that relatively simple crystal chemical principles are useful guides for predicting the relevant equilibrium stable isotope fractionation factors. Foremost among the factors controlling fractionation are the effects of charge and coordination number on bond lengths. Nonetheless, advancements in theoretical treatments and in experimental methods have been necessary to place interpretations of variations in the isotope ratios of Mg, Si, Fe, Ni, and other non-traditional stable isotope systems, on a quantitative footing. The feedback between basic crystal chemical considerations, *ab initio* calculations, experiments, and measurements in well-characterized natural samples has proven most effective in establishing reliable equilibrium fractionation factors.

Acknowledgments

Funding for the UCLA research described here has come from the National Science Foundation (EAR-0711411) and NASA (NNX10A175G). A.S. acknowledges support from NSF (EAR-1321858). Reviews by three anonymous reviewers and the editor improved the presentation and are greatly appreciated by the authors.

References

Beard, B.L., Johnson, C.M., 2004. Inter-mineral Fe isotope variations in mantle-derived rocks and implications for the Fe geochemical cycle. Geochim. Cosmochim. Acta 68, 4727–4743.
Beard, B.L., Johnson, C.M., 2007. Comment on "Iron isotope fractionation during planetary differentiation" by S. Weyer et al., Earth Planet. Sci. lett. V240, pages 251–264. Earth Planet. Sci. Lett. 256, 633–637.
Bigeleisen, J., Mayer, M.G., 1947. Calculation of equilibrium constants for isotopic exchange reactions. J. Chem. Phys. 15 (5), 261–267.
Birch, F., 1964. Elasticity and constitution of the Earth's interior. J. Geophyhs. Res. 69, 4377–4388.
Blanchard, M., Poitrasson, F., Méheut, M., Lazzeri, M., Mauri, F., Balan, E., 2009. Iron isotope fractionation between pyrite (FeS_2), hematite (Fe_2O_3) and siderite ($FeCO_3$): a first-principles density functional theory study. Geochim. Cosmochim. Acta 73, 6565–6578.
Born, M., Mayer, J.E., 1932. Zur Gittertheorie der ionenkristalle. Z. Phys. 75 (1), 1–18.
Bourdon, B., Tipper, E.T., Fitoussi, C., Stracke, A., 2010. Chondritic Mg isotope composition of the Earth. Geochim. Cosmochim. Acta 74, 5069–5083.
Burdett, J.K., Hawthorne, F.C., 1993. An orbital approach to the theory of bond valance. Am. Mineral. 78, 884–892.
Burdett, J.K., McLarnan, T.J., 1984. An orbital interpretation of Pauling's rules. Am. Mineral. 69, 601–621.
Cao, X., Liu, Y., 2011. Equilibrium mass-dependent fractionation relationships for triple oxygen isotopes. Geochim. Cosmochim. Acta 75, 7435–7445.
Chakrabati, R., Jacobsen, S.B., 2010. The isotopic composition of magnesium in the inner solar system. Earth Planet. Sci. Lett. 293, 349–358.
Clayton, R.N., Goldsmith, J.R., Karel, K.J., Mayeda, T.K., Newton, R.C., 1975. Limits on the effect of pressure on isotopic fractinoation. Geochim. Cosmochim. Acta 39, 1197–1201.
Corgne, A., Shantanu, K., Wood, B.J., McDonough, W.F., Fei, Y., 2008. Metal-silicate partitioning and constraints on core composition and oxygen fugacity during Earth accretion. Geochim. Cosmochim. Acta 72, 574–589.
Dauphas, N., Craddock, P.R., Asimow, P.D., Bennett, V.C., Nutman, A.P., Ohnenstetter, D., 2009. Iron isotopes may reveal the redox conditions of mantle melting from Archean to Present. Earth Planet. Sci. Lett. 288, 255–267.

Dauphas, N., Roskosz, M., Alp, E.E., Sio, C.K., Tissot, F.L.H., Neuville, D., Hu, M., Zhao, J., Tissandier, L., Médard, E., 2012. Iron isotope goechemistry with a synchrotron light beam. Goldschmidt 2012, Montreal, 1626 l.
Detraux, F., Gonze, X., 2001. Photoelasticity of a-quartz from first principles. Phys. Rev. B 63, 115118.
Fitoussi, C., Bourdon, B., 2012. Silicon isotope evidence against an enstatite chondrite Earth. Science 335, 1477–1480.
Frey, F.A., Prinz, M., 1978. Ultramafic inclusions from San Carlos, Arizona: petrologic and geochemical data bearing on their petrogenesis. Earth Planet. Sci. Lett. 38, 129–176.
Fujino, K., Sasaki, S., Takeuchi, Y., Sadanaga, R., 1981. X-ray determination of electron distributions in forsterite, fayalite and tephroite. Acta Crystallogr. B37, 513–518.
Georg, R.B., 2006. Geochemistry of stable silicon isotopes measured by high-resolution multi-collector inductively-coupled-plasma mass spectrometry (HR-MC-ICP-MS). Swiss Federal Institute of Technology Zürich, Zürich, p. 144 (Dr. Sc. Thesis).
Georg, R.B., Halliday, A.N., Schauble, E.A., 2007. Silicon in Earth's core. Nature 447, 1102–1106.
Gibbs, G.V., Ross, N.L., Cox, D.F., Rosso, K.M., 2014a. Insights into the crystal chemistry of Earth materials rendered by electron density distributions: Pauling's rules revisited. Am. Mineral. 99, 1071–1084.
Gibbs, G.V., Ross, N.L., Cox, D.F., Rosso, K.M., Iverson, B.B., Spackman, M.A., 2014b. Pauling bond strength, bond length and electron density distribution. Phys. Chem. Miner. 41, 17–25.
Grüneisen, E., 1912. Theorie des festen Zustandes einatomiger Elemente. Ann. Phys. 39, 257–306.
Handler, M.R., Baker, J.A., Schiller, M., Bennett, V.C., Yaxley, G.M., 2009. Magnesium stable isotope composition of Earth's upper mantle. Earth Planet. Sci. Lett. 282, 306–313.
Hazen, R.M., 1988. A useful fiction: polyhedral modeling of mineral properties. Am. J. Sci. 288-A, 242–269.
Hill, P.S., Schauble, E.A., Shahar, A., Tonui, E., Young, E.D., 2009. Experimental studies of equilibrium iron isotope fractionation in ferric aquo-chloro complexes. Geochim. Cosmochim. Acta 73, 2366–2381.
Hill, P.S., Schauble, E.A., Young, E.D., 2010. Effects of changing solution chemistry on Fe^{3+}/Fe^{2+} isotope fractionation in aqueous Fe-Cl solutions. Geochim. Cosmochim. Acta 74, 6669–6689.
Hin, R.C., Schmidt, M.W., Bourdon, B., 2012. Experimental evidence for the absence of iron isotope fractionation between metal and silicate liquids at 1 GPa and 1250 to 1300 °C and its cosmochemical consequences. Geochim. Cosmochim. Acta 93, 164–181.
Hin, R.C., Fitoussi, C., Schmidt, M.W., Bourdon, B., 2014. Experimental determination of the Si isotope fractionation factor between liquid metal and liquid silicate. Earth Planet. Sci. Lett. 387, 55–66.
Horita, J., Driesner, T., Cole, D.R., 1999. Pressure effect on hydrogen isotope fractionation between brucite and water at elevated temperatures. Science 286, 1545–1547.
Jackson, W.E., Farges, F., Yeager, M., Mabrouk, P.A., Rossano, S., Waychunbas, G.A., Solomon, E.I., Brown, G.E.J., 2005. Multi-spectroscopic study of Fe(II) in silicate glasses: implications for the coordination environment of Fe(II) in silicate melts. Geochim. Cosmochim. Acta 69, 4315–4332.
Jeffcoate, A.B., Elliot, T., Kasemann, S.A., Ionov, D., Cooper, K., Brooker, R., 2007. Li isotope fractionation in peridotites and mafic melts. Geochim. Cosmochim. Acta 71 (1), 202–218.
Johnson, C.M., McLennan, S.M., McSween, H.Y., Summons, R.E., 2013. Smaller, better, more: five decades of advances in geochemistry. In: Bickford, M.E. (Ed.), Advances, Impacts, and Interactons: Geological Society of America Special Paper 500. The Geological Society of America, pp. 1–44.
Jordan, M.K., Young, E.D., 2014. Equilibrium metal-silicate Fe isotope fractionation and the implications for differentiation in planetary bodies. 45th Lunar and Planetary Science Conference, The Woodlands, Texas, 2318l.
Kieffer, S.W., 1979. Thermodynamics and lattice vibrations of minerals: 1. Mineral heat capacities and their relationships to simple lattice vibrational models. Rev. Geophys. Space Phys. 17 (1), 1–19.
Kieffer, S.W., 1982. Thermodynamics and lattice vibrations of minerals: 5. Applications to phase equilibria, isotope fractionation, and high-pressure thermodynamic properties. Rev. Geophys. Space Phys. 20, 827–849.
Kirfel, A., Lippmann, T., Blaha, P., Schwarz, K., Cox, D.F., Rosso, K.M., Gibbs, G.V., 2005. Electron density distribution and bon critical point properties for forsterite, Mg_2SiO_4, determined with synchrotron single crystal X-ray diffracton data. Phys. Chem. Miner. 32, 301–313.
Kugel, G., Carabatos, C., Hennion, B., Prevot, B., Revcolevschi, A., Tocchetti, D., 1977. Lattice dynamics of wustite (FeO). Phys. Rev. B 16, 378–385.
Kuroda, Y., Hariya, Y., Suzuoki, T., Matsuo, S., 1982. D/H fractionation between water and melts of quartz, K-feldspar, albite and anorthite at high temperature and pressure. Geochem. J. 16, 73–78.
Lazar, C., Young, E.D., Manning, C.E., 2012. Experimental determination of equilibrium nickel isotope fractionation between metal and silicate from 500 C to 950 C. Geochim. Cosmochim. Acta 86, 276–295.
Li, J., Struzhkin, V.V., Mao, H.-K., Shu, J., Hemley, R.J., Fei, Y., Mysen, B., Dera, P., Prakapenka, V., Shen, G., 2004. Electronic spin state of iron in lower mantle perovskite. Proc. Natl. Acad. Sci. 101 (39), 14027–14030.
Lin, J.-F., Struzhkin, V.V., Jacobsen, S.D., Hu, M.Y., Chow, P., Kung, J., Liu, H., Mao, H.-K., Hemley, R.J., 2005. Spin transition of iron in magnesiowüstite in the Earth's lower mantle. Nature 436, 377–380.
Liu, S.A., Teng, F.Z., Yang, W., Wu, F.Y., 2011. High-temperature inter-mineral magnesium isotope fractionation in mantle xenoliths from the North China craton. Earth Planet. Sci. Lett. 308, 131–140.
Macris, C.A., Young, E.D., Manning, C.E., 2013. Experimental determination of equilibrium magnesium isotope fractionation between spinel, forsterite, and magnesite from 600 to 800° C. Geochim. Cosmochim. Acta 118, 18–32.
Macris, C.A., Manning, C.E., Young, E.D., 2015. Crystal chemical constraints on inter-mineral Fe isotope fractionation and implications for Fe isotope disequilibrium in San Carlos mantle xenoliths. Geochim. Cosmochim. Acta (in press).
Matsuhisa, J., Goldsmith, J.R., Clayton, R.N., 1978. Mechanisms of hydrothermal crystallisation of quartz at 250 C and 15 kbar. Geochim. Cosmochim. Acta 42, 173–182.
McDonough, W.F., 2003. Compositional model for the Earth's core. In: Holland, H.D., Turekian, K.K. (Eds.), Treatise on Geochemistry Volume 2: The Mantle and Core. Elsevier, pp. 547–568.
Méheut, M., Schauble, E.A., 2014. Silicon isotope fractionation in silicate minerals: insights from first-principles models of phyllosilicates, albite and pyrope. Geochim. Cosmochim. Acta 134, 137–154.
Méheut, M., Lazzeri, M., Balan, E., Mauri, F., 2009. Structural control over equilibrium silicon and oxygen isotopic fractionation: a first-principles density-functional theory study. Chem. Geol. 258 (1–2), 28–37.
Murphy, C.A., Jackson, J.M., Sturhahn, W., 2013. Experimental constraints on the thermodynamics and sound velocities of hcp-Fe to core pressures. J. Geophys. Res. Solid Earth 118, 1999–2016.
Northrop, D.A., Clayton, R.N., 1966. Oxygen isotope fractionations in systems containing dolomite. J. Geol. 74, 174–196.
O'Neil, J.R., 1986. Theoretical and experimental aspects of isotopic fractionation. In: Valley, J.W., Taylor, H.P., O'Neil, J.R. (Eds.), Stable Isotopes in High Temperature Geological Processes 16. Mineralogical Society of America, Chelsea, pp. 1–40.
Pauling, L., 1929. The principles determining the structure of complex ionic crystals. J. Am. Chem. Soc. 51, 1010–1026.
Pauling, L., 1960. The Nature of the Chemical Bond. Cornell University Press, Ithaca.
Pauling, L., 1980. The nature of silicon-oxygen bonds. Am. Mineral. 65, 321–323.
Pogge von Strandmann, P.A.E., Elliot, T., Marschall, H.R., Coath, C., Lai, Y.-J., Jeffcoate, A., ionov, D., 2011. Variations of Li and Mg isotope ratios in bulk chondrite and mantle xenoliths. Geochim. Cosmochim. Acta 75, 5247–5268.
Poitrasson, F., 2007. Does planetary differentiation really fractionate iron isotopes? Earth Planet. Sci. Lett. 256, 484–492.
Poitrasson, F., Halliday, A.N., Lee, D.-C., Levasseur, S., Teutsch, N., 2004. Iron isotope differences between Earth, Moon, Mars and Vesta as possible records of contrasted accretion mechanisms. Earth Planet. Sci. Lett. 223, 253–266.
Poitrasson, F., Roskosz, M., Corgne, A., 2009. No iron isotope fractionation between molten alloys and silicate melt to 2000 C and 7.7 GPa: experimental evidence and implications for planetary differentiation and accretion. Earth Planet. Sci. Lett. 278, 376–385.
Polyakov, V.B., 1997. Equilibrium fractionation of the iron isotopes: estimation from Mossbauer spectroscopy data. Geochim. Cosmochim. Acta 61, 4213–4217.
Polyakov, V.B., 2009. Equilibrium iron isotope fractionation at core–mantle boundary conditions. Science 323, 912–914.
Polyakov, V.B., Mineev, S.D., 2000. The use of Mössbauer spectroscopy in stable isotope geochemistry. Geochim. Cosmochim. Acta 64, 849–865.
Polyakov, V.B., Clayton, R.N., Horita, J., Mineev, S.D., 2007. Equilibrium iron isotope fractionation factors of minerals: reevaluation from the data of nuclear inelastic resonant X-ray scattering and M ssbauer spectroscopy. Geochim. Cosmochim. Acta 71, 3833–3846.
Pupyshev, V.I., Panchenko, Y.N., Stepanov, N.F., 1994. A new derivation for the Teller–Redlich isotopic product rule. Vib. Spectrosc. 7, 191–196.
Richet, P., Bottinga, Y., Javoy, M., 1977. A review of hydrogen, carbon, nitrogen, oxygen, sulphur, and chlorine stable isotope fractionation among gaseous molecules. Ann. Rev. Earth Planet. Sci. 5, 65–110.
Rudnick, R.L., Ionov, D.A., 2007. Lithium elemental and isotopic disequilibrium in minerals from peridotite xenoliths from far-east Russia: product of recent melt/fluid–rock reaction. Earth Planet. Sci. Lett. 256, 278–293.
Rustad, J.R., Yin, Q.-Z., 2009. Iron isotope fractionation in the Earth's lower mantle. Nat. Geosci. 2, 514–518.
Rustad, J.R., Casey, W.H., Yin, Q.-Z., Bylaska, E.J., Felmy, A.R., Bogatko, S.A., Jackson, V.E., Dixon, D.A., 2010. Isotopic fractionation of Mg2 + (aq), Ca2 + (aq), and Fe2 + (aq) with carbonate minerals. Geochim. Cosmochim. Acta 74, 6301–6323.
Savage, P.S., Armytage, R.M.G., Georg, R.B., Halliday, A.N., 2014. High temperature silicon isotope geochemistry. Lithos 190–191, 500–519.
Schauble, E., 2004. Applying stable isotope fractionation theory to new systems. In: Johnson, C.M., Beard, B., Albarede, F. (Eds.), Reviews in Mineralogy & Geochemistry, v. 56, Geochemistry of Non-traditional Stable Isotopes. Mineralogical Society of America.
Schauble, E.A., 2011. First-principles estimates of equilibrium magnesium isotope fractionation in silicate, oxide, carbonate and hexaaquamagnesium (2+) crystals. Geochim. Cosmochim. Acta 75, 844–869.
Schoenberg, R., von Blanckenburg, F., 2006. Modes of planetary-scale Fe isotope fractionation. Earth Planet. Sci. Lett. 252, 342–359.
Schuessler, J.A., Schoenberg, R., Behrens, H., von Blanckenburg, F., 2007. The experimental calibration of the iron isotope fractionation factor between pyrrhotite and peralkaline rhyolitic melt. Geochim. Cosmochim. Acta 71, 417–433.
Shahar, A., Young, E.D., Manning, C.E., 2008. Equilibrium high-temperature Fe isotope fractionation between fayalite and magnetite: an experimental calibration. Earth Planet. Sci. Lett. 268, 330–338.
Shahar, A., Ziegler, K., Young, E.D., Ricolleau, A., Schauble, E.A., Fei, Y.W., 2009. Experimentally determined Si isotope fractionation between silicate and Fe metal and implications for Earth's core formation. Earth Planet. Sci. Lett. 288, 228–234.
Shahar, A., Hillgren, V.J., Young, E.D., Fei, Y., Macris, C.A., Dent, L., 2011. High-temperature Si isotope fractionation between iron metal and silicate. Geochim. Cosmochim. Acta 75, 7688–7697.
Shahar, A., Hillgren, V.J., Horan, M.F., Mesa-Garcia, J., Kaufman, L.A., Mock, T.D., 2014. Sulfur-controlled iron isotope fractionation experiments of core formation in planetary bodies. Geochim. Cosmochim. Acta (in press).

Shannon, R.D., 1976. Revised effective ionic radii and systematic studies of interatomic distances in halides and chalcogenides. Acta Crystallogr. A 32 (5), 751–767.
Stewart, R.F., Whitehead, M.A., Donnay, G., 1980. The ionicity of the Si–O bond in low-quartz. Am. Mineral. 65, 324–326.
Telus, M., Dauphas, N., Moynier, F., Tissot, F.L.H., Teng, F.-Z., Nabelek, P.I., Craddock, P.R., Groat, L.A., 2012. Iron, zinc, magnesium and uranium isotopic fractionation during continental crust differentiation: the tale from migmatites, granitoids, and pegmatites. Geochim. Cosmochim. Acta 97, 247–265.
Teng, F.Z., Yang, W., Rudnick, R.L., Hu, Y., 2013. Heterogeneous magnesium isotopic composition of the lower continental crust: a xenolith perspective. Geochem. Geophys. Geosyst. 14 (9).
Urey, H.C., 1947. The thermodynamic properties of isotopic substances. J. Chem. Soc. 562–581.
Wade, J., Wood, B.J., 2005. Core formation and the oxidation state of the Earth. Earth Planet. Sci. Lett. 236, 78–95.
Wang, K., Moynier, F., Dauphas, N., Barrat, J.-A., Craddock, P., Sio, C.K., 2012. Iron isotope fractionation in planetary crusts. Geochim. Cosmochim. Acta 89, 31–45.
Weyer, S., Ionov, D.A., 2007. Partial melting and melt percolation in the mantle: the message from Fe isotopes. Earth Planet. Sci. Lett. 259, 119–133.
Weyer, S., Anbar, A.D., Brey, G.P., Munker, C., Mezger, K., Woodland, A.B., 2005. Iron isotope fractionation during planetary differentiation. Earth Planet. Sci. Lett. 240, 251–265.
Weyer, S., Anbar, A.D., Brey, G.P., Muncker, C., Woodland, A.B., 2007. Fe-isotope fractionation during partial melting on Earth and the current view on the Fe-isotope budgets of the planets (reply to the comment of F. Poitrasson and to the comment by B.L. Beard and C.M. Johnson on "Iron isotope fractionation during planetary differentiation" by S. Weyer, A.D. Anbar, G.P. Brey, C. Munker, K. Mezger, and A.B. Woodland). Earth Planet. Sci. Lett. 256, 638–646.
Wiechert, U.H., Halliday, A.N., 2007. Non-chondritic magnesium and the origins of the inner terrestrial planets. Earth Planet. Sci. Lett. 256, 360–371.
Wilke, M., Schmidt, C., Farges, F., Malavergne, V., Gautron, L., Simionovici, A., Hahn, M., 2006. Structural environment of iron in hydrous aluminosilicate glass and melt — evidence from X-ray absorption spectroscopy. Chem. Geol. 229, 55–67.
Williams, H.M., Bizimis, M., 2014. Iron isotope tracing of mantle heterogeneity within the source regions of oceanic basalts. Earth Planet. Sci. Lett. 404, 396–407.
Williams, H.M., McCammon, C.A., Peslier, A.H., Halliday, A.N., Teutsch, N., Levasseur, S., Burg, J.P., 2004. Iron isotope fractionation and oxygen fugacity of the mantle. Science 304, 1656–1659.
Williams, H.M., Peslier, A.H., McCammon, C.A., Halliday, A.N., Levasseur, S., Teutsch, N., Burg, J.P., 2005. Systematic iron isotope variations in mantle rocks and minerals: the effects of partial melting and oxygen fugacity. Earth Planet. Sci. Lett. 235, 435–452.
Williams, H.M., Nielsen, S.G., Renac, C., Griffin, W.L., O'Reilly, S.Y., McCammon, C.A., Pearson, N., Viljoen, F., Alt, J.C., Halliday, A.N., 2009. Fractionation of oxygen and iron isotopes by partial melting processes: implications for the interpretation of stable isotope signatures in mafic rocks. Earth Planet. Sci. Lett. 283, 155–166.
Williams, H.M., Wood, B.J., Wade, J., Frost, D.J., Tuff, J., 2012. Isotopic evidence for internal oxidation of the Earth's mantle during accretion. Earth Planet. Sci. Lett. 321–322, 54–63.
Wood, B.J., 2008. Accretion and core formation: constraints from metal-silicate partitioning. Philos. Trans. R. Soc. Lond. A 366, 4339–4355.
Xiao, Y., Teng, F.-Z., Zhang, H.-F., Yang, W., 2013. Large magnesium isotope fractionation in peridotite xenoliths from eastern North China craton: product of melt–rock interaction. Geochim. Cosmochim. Acta 115, 241–261.
Young, E.D., Galy, A., Nagahara, H., 2002. Kinetic and equilibrium mass-dependent isotope fractionation laws in nature and their geochemical and cosmochemical significance. Geochim. Cosmochim. Acta 66 (6), 1095–1104.
Young, E.D., Tonui, E., Manning, C.E., Schauble, E.A., Macris, C.A., 2009. Spinel-olivine magnesium isotope thermometry in the mantle and implications for the Mg isotopic composition of Earth. Earth Planet. Sci. Lett. 288, 524–533.
Zerr, A., Diegeler, A., Boehler, R., 1998. Solidus of Earth's deep mantle. Science 281, 243–246.
Zhao, X., Zhang, H., Zhu, X., Tang, S., Tang, Y., 2010. Iron isotope variations in spinel peridotite xenoliths from North China Craton: implications for mantle metasomatism. Contrib. Mineral. Petrol. 160, 1–14.
Zhao, X., Zhang, H., Zhu, X., Tang, S., Yan, B., 2012. Iron isotope evidence for multistage melt–peridotite interactions in the lithospheric mantle of eastern China. Chem. Geol. 292, 127–139.
Zhu, X.K., Guo, Y., Williams, R.J.P., O'Neil, J.R., Matthews, A., Belshaw, N.S., Canters, G.W., de Waal, E.C., Weser, U., Burgess, B.K., Salvato, B., 2002. Mass fractionation processes of transition metal isotopes. Earth Planet. Sci. Lett. 200, 47–62.
Ziegler, K., Young, E.D., Schauble, E.A., Wasson, J.T., 2010. Metal–silicate silicon isotope fractionation in enstatite meteorites and constraints on Earth's core formation. Earth Planet. Sci. Lett. 295, 487–496.